International Journal of Solids and Structures 47 (2010) 1618–1640

Contents lists available at ScienceDirect

International Journal of Solids and Structures

journal homepage: www.elsevier.com/locate/ijsolstr

Shape optimization and its extension to topological design based on isogeometric analysis

Yu-Deok Seo, Hyun-Jung Kim, Sung-Kie Youn *

Department of Mechanical Engineering, Korea Advanced Institute of Science and Technology, 373-1, Guseong-dong, Yuseong-gu, Daejeon 305-701, Republic of Korea

ARTICLE INFO

Article history:
Received 16 September 2009
Received in revised form 25 January 2010
Available online 11 March 2010

Keywords:
Shape optimization
Topology optimization
NURBS (Non-Uniform Rational B-Spline)
Isogeometric analysis
Trimmed surface analysis

ABSTRACT

In most of structural optimization approaches, finite element method (FEM) has been employed for structural response analysis and sensitivity calculation. However, the approaches generally suffer certain drawbacks. In shape optimization, cumbersome parameterization of design domain is required and time consuming remeshing task is also necessary. In topology optimization, design results are generally restricted on the initial design space and additional post-processing is required for communication with CAD systems. These drawbacks are due to the use of different mathematical languages in design or geometric modeling and numerical analysis: spline basis functions are used in design and geometric modeling whereas Lagrangian and Hermitian polynomials in analysis. Isogeometric analysis is a very attractive and promising alternative to overcome the limitations resulting from the use of the conventional FEM in structural optimization. In isogeometric analysis, the same spline information such as control points and spline basis functions which represent geometries in CAD systems are also used in numerical analysis. Such unification of the mathematical languages in CAD, analysis and design optimization can resolve the issues mentioned above. In this work, structural shape optimization using isogeometric analysis is studied on 2D and shell problems. The proposed framework is extended to topology optimization using trimming techniques. New inner fronts are introduced by trimming spline curves in topology optimization. Trimmed surface analysis which was recently proposed to analyze arbitrary complex topology problems is employed for topology optimization. Some benchmarking problems in shape and topology optimization are treated using the proposed approach.

1. Introduction

Remarkable progress has been achieved in shape and topology optimization during the past three decades. Shape and topology optimization are concerned with finding optimal shape and topology of a structure by the iterative process based on structural response analysis and sensitivity calculation, in case of gradient-based optimization methods. In most of structural optimization approaches, finite element method (FEM) has been employed for structural response analysis and sensitivity calculation.

In the conventional shape optimization, the adequate choices of boundary representation and design variables are essential for the success of the optimization. In the early days of shape optimization, the coordinates of the boundary nodes of a finite element model were used as design variables (Francavilla et al., 1975). Using nodal coordinates as design variables is very intuitive and directly related to the finite element method. However, such design variables lead to unrealistic designs due to irregular boundaries, difficulty for maintaining adequate finite element mesh and the excessive number of design variables (Braibant and Fleury, 1984; Haftka and Grandhi, 1986; Ding, 1986; Hsu, 1994). To guarantee the smoothness of boundaries, many researchers paid attentions on the polynomial representation of boundaries (Bhavikatti and Ramakrishnan, 1980; Pedersen and Laursen, 1983). The coefficients of polynomials were used as design variables in their approaches. Although the polynomial boundary representation gives sufficient smoothness, impractical oscillatory boundaries were observed in higher order polynomial. Another problem in the approach is the lack of local control since the change of one coefficient of the polynomial alters the whole shape of curve. Splines such as B-spline and NURBS could eliminate the oscillatory boundary and be locally controlled with high degree of smoothness. Thus, the spline boundary representation became the most popular geometrical representation in shape optimization. Due to the use of splines in geometric description, the geometric design model based on splines and analysis model based on finite elements are completely separated. Therefore, a parameterization between design variables and finite element model is required during the optimization process to define the relation between design and analysis models. Another issue in shape optimization is to maintain an adequate finite element model during the iterative process. For this, design element concept (Imam, 1982),

* Corresponding author. Tel.: +82 42 350 3034; fax: +82 42 350 3210.
E-mail address: skyoun@kaist.ac.kr (S.-K. Youn).

0020-7683/$ - see front matter © 2010 Elsevier Ltd. All rights reserved.
doi:10.1016/j.ijsolstr.2010.03.004

adaptive meshing (Bennet and Botkin, 1984) and remeshing (Wilke et al., 2006) techniques were used. A comprehensive review of the early development of shape optimization can be found in the survey literatures (Braibant and Fleury, 1984; Haftka and Grandhi, 1986; Ding, 1986; Hsu, 1994). In contrast to the early works of shape optimization, Kim and Chang (2005) proposed fixed grid based shape optimization inspired from topology optimization techniques. They called their approach Eulerian shape optimization because computational finite element mesh is fixed during the optimization process.

Since initially given topologies cannot be changed in shape optimization, optimal designs are highly dependent on initial shape and topologies. In order to overcome the restriction on the given topologies in shape optimization, topology optimization which enables to describe the changes in topology has received great deal of attention. The first attempt was made by Bendsoe and Kikuchi (1988). In their works, the homogenization method (Bendsoe and Kikuchi, 1988; Bendsoe and Sigmund, 2003) and SIMP (Solid Isotropic Material with Penalization) method (Bendsoe and Sigmund, 2003; Rozvany et al., 1992; Bendsoe and Sigmund, 1999) were developed. The former employs homogenization concept on micro-structure to represent lay out of the material and void region. The latter uses the relationship between material properties and element density to be optimized. In SIMP method, the final optimization problem can be stated as finding the optimum distribution of element densities in the structure. SIMP method is easy to implement and efficient due to good harmony with FEM and thus has been widely used in a broad range of engineering design problems such as linear elastic, dynamics, fluid mechanics and multi-physics. The numerous works on the conventional topology optimization can be found in (Bendsoe and Sigmund, 2003) the references therein. SIMP method has its inherent numerical instabilities such as checker-board patterns, mesh dependency and minimum member size control, although they can be avoided by several techniques and constraints: density or sensitivity filtering (Sigmund and Petersson, 1998; Bruns and Tortorelli, 2001; Bourdin, 2001; Guo and Gu, 2004), the perimeter control (Haber et al., 1996), the slope constraint (Petersson and Sigmund, 1998; Borrvall, 2001; Zhou et al., 2001) and density redistribution (Youn and Park, 1997).

For new attempts for topology optimization, various methods have been developed. Xie and Steven proposed the evolutionary structural optimization (ESO) based on element-wise stress level (Xie and Steven, 1993; Xie and Steven, 1994; Querin et al., 1998; Kim et al., 2003). In the ESO, optimal topology of a structure can be represented by adding and/or subtracting elements. Yoon and Kim (2005) proposed a new topology optimization methodology named element connectivity parameterization (ECP). In the ECP, the elastic links are assumed to exist at vertices of elements and employed as design variables to determine existence of elements connected by them. The ECP can provide excellent designs in geometrically nonlinear problems since unrealistic effect on distortion of low density elements is eliminated. The material cloud (MC) method was proposed by Chang and Youn (2006). The optimal topology is expressed by means of the material clouds and the size and/or position of them are design variables in the material cloud method based topology optimization. With the method, the change of design space can be easily achieved and computational costs can be reduced by introducing the active finite elements.

Topology optimization methods described so far represent the optimal topology with cells or elements. Since such cell-based representation of topology leads irregular and vague boundary layouts, new attempts for smooth and definite material boundary have been studied. In recent years, level set based topology optimization which was first proposed by Sethian and Wiegmann (2000) has been extensively investigated. The moving front which express material boundary is adopted as design variables. The evolution of material boundary is governed by Hamilton–Jacobi equation employing the shape velocity computed from design sensitivity analysis. Several works on level set based shape and topology optimization can be found in (Allaire et al., 2004; Allaire and Jouve, 2005; Amstutz and Andra, 2006; Wang et al., 2003; Wang and Wang, 2004; Wang et al., 2004). Despite the profound investigations on level set based topology optimization, it has a shortcoming which is concerned with the incapability of creating new inner fronts during the optimization process. Due to the shortcoming, an initial level set generally includes a number of inner fronts so that the optimum topology of level set based topology optimization is highly dependent on the initial number and positions of inner fronts. In order to overcome the shortcoming, level set based topology optimization attempts for free creation of new inner fronts based on the topological derivative (Burger et al., 2004; Allaire and Jouve, 2005; Amstutz and Andra, 2006) and the strain energy density (Park and Youn, 2008) have been presented. Belytschko et al. (2003) proposed a nodal implicit function based topology optimization using level set representation and extended finite element method (XFEM). There has been several works on spline based topology optimization. The earliest spline based topology optimization is the bubble method (Eschenauer et al., 1993). Inserting bubbles based on the characteristic function and shape optimization of the outer boundaries and inner bubbles which are represented by splines are sequentially repeated for topology optimization in the method. The conventional FEM with remeshing scheme is used for analysis in the method. Cervera and Trevelyan (2005) proposed a spline based topology optimization approach using BEM (boundary element method) in evolutionary concept. In their work, boundaries are represented by NURBS and positions of the control points are design variables. Then, the direction and amount of movements of the control points are determined based on the stress of boundary elements calculated by BEM. New inner fronts are created at lower stress region by taking the internal evaluation points surrounding the region as control points of the inner fronts. Lee et al. (2007) proposed a spline based topology optimization approach using fixed FE grid. Design variables are the control points of the boundaries and inner fronts. The inner fronts are introduced based on the topological derivative. They also proposed the selection criteria, which is defined in the ratio of sensitivity of an objective function and that of a constraint, as a measure for taking topological changes.

Despite rapid and wide advances in topology optimization, most of topology optimization methods suffer from FEM related problems. In general, they use a fixed FE grid for numerical analysis, thus design results are highly dependent on the initial fixed computational mesh. Although the studies on design space expansion were presented in 2D problems (Chang and Youn, 2006; Jang and Kwak, 2008), the initial grid dependency problem is very difficult to resolve in optimization of shell problems. Moreover, the topology optimization methods which use cell-based representation such as SIMP, ESC, ECP and MC, etc. require additional postprocessing effort to produce CAD data of the optimal designs.

As mentioned above, shape and topology optimization methods have the FEM related shortcomings such as additional parameterization and troublesome remeshing in shape optimization and dependency on the initial FE grid and huge effort for postprocessing in topology optimization. Main reason of the shortcomings is the use of different mathematical languages in geometric design and analysis, i.e. splines in design whereas polynomials in analysis. Such inconsistent mathematical languages in geometric description and numerical analysis are the causes of serious problems in a typical product development process. In most of CAD and CAE systems, the geometric design module and the numerical analysis module are operated completely separated with different mathematical representation of the same object. However, intensive

interaction or communication between these modules is desirable due to the iterative nature of the development process. Modification of design resulting from the analysis is frequently required to improve quality and performance of products. However, such an inconvenient communication between the two modules causes loss of accuracy, waste of manpower and time.

As the demand on convenient and efficient communication between design and analysis increases, there have been many attempts to unify the mathematical languages in design and analysis by using splines. Kagan et al. (1998) proposed new B-spline finite elements in linear elastic problems. Cho and Roh (2003), Roh and Cho (2004) discussed the finite element method using B-spline for a shell analysis. Subsequently, they proposed the integrated approach of design and analysis with B-spline basis functions (Roh and Cho, 2005). Subbarayan and his co-workers (Natekar et al., 2004; Rayasam et al., 2007) proposed Constructive Solid Analysis (CSA) inspired from Constructive Solid Geometry based on Boolean operation in CAD systems. They used NURBS (Non-Uniform Rational B-Spline) basis functions to represent boundaries and field variables. They extended their works to optimal shape design by changing geometric variables of the primitives which are used in composition of geometries (Zhang et al., 2007a). Hughes et al. (2005) have come up with the name "isogeometric analysis" in which NURBS are used for modeling and analysis. They proposed the framework of direct use of spline data provided from CAD systems in numerical analysis by refinement operation from coarse mesh. Also, further studies on isogeometric analysis have been done by the same group (Cottrell et al., 2006; Bazilevs et al., 2007; Cottrell et al., 2007; Zhang et al., 2007b). Several works on isogeometric analysis using T-spline were presented to improve geometrical stability and numerical efficiencies (Uhm et al., 2008; Dörfel et al., 2010; Bazilevs et al., 2010). Recently, the trimmed surface analysis (Kim et al., 2009) was proposed to treat arbitrary complex topology surfaces without dividing the model into multiple tensor-product patches which requires huge modeling effort and time. By using the isogeometric analysis, the communication between CAD systems and analysis becomes very easy and efficient. Moreover, the isogeometric analysis is superior in numerical accuracy since geometries are exactly represented by splines whereas geometries are approximated in conventional FEM (Bazilevs et al., 2007).

By using the same mathematical language, i.e. splines, in design optimization, any additional parameterization between design variables and analysis model becomes unnecessary. As a shape of surface changes by the movements of control points, the mesh of the surface which is embedded in the geometry also changes automatically. Therefore remeshing is not required during the entire optimization process. In addition, design result is not dependent on the initial design space. Some researchers have been contributed to shape optimization with isogometric analysis (Seo and Youn, 2008; Wall et al., 2008; Cho and Ha, 2009) but there have been no attempts to apply the isogeometric analysis to topology optimization.

In the present work, shape and topology optimization using isogeometric analysis is presented as the first step for a spline based integrated shape and topology optimization approach. Shape optimization of 2D and shell problems is treated and the same framework is extended to topological design by using the trimmed surface analysis.

Definitions and properties of B-spline, NURBS and T-spline are briefly reviewed in Section 2. Isogeometric analysis and the trimmed surface analysis are described in Section 3. Derivation of analytic sensitivities of objective functions such as compliance and maximum stress is presented in Section 4. Numerical examples on shape optimization using isogeometric analysis are presented in Section 5. Extension to topology optimization is followed in Section 6. Final conclusion and future works are addressed in Section 7.

2. B-spline, NURBS and T-splines

In this section, definitions of B-spline and basis functions are briefly introduced. Knot insertion which is a fundamental and essential geometric operation in spline and isogeometric analysis is explained. Then, NURBS and T-spline are also explained.

2.1. B-spline basis functions

B-spline basis functions are defined by the knot vector which is a set of non-decreasing parameters of real number (knots). Let a knot vector $\mathbf{s} = [s_0, s_1, \ldots, s_{n+p}]$ where n is the number of control points and p the degree of B-spline basis functions. The interval $[s_0, s_{n+p}]$ is called a *patch*, and the interval $[s_i, s_{i+1}]$ is called a *knot span*. Non-zero knot spans of a knot vector are piecewise defined segments or elements in the parametric space. It is called an *open* knot vector if its first and last knots are repeated $p+1$ times whereas a *closed* knot vector otherwise. A B-spline defined by an open knot vector interpolates both end control points while it does not interpolate with a closed knot vector.

Then, B-spline basis function can be determined by the following recursive formula starting with piecewise constant:

$$\begin{aligned} N_{i,0}(s) &= \begin{cases} 1, & s_i \leqslant s < s_{i+1} \\ 0, & \text{otherwise} \end{cases} \\ N_{i,p}(s) &= \frac{s - s_i}{s_{i+p} - s_i} N_{i,p-1}(s) + \frac{s_{i+p+1} - s}{s_{i+p+1} - s_{i+1}} N_{i+1,p-1}(s) \end{aligned} \tag{1}$$

Important properties of B-spline basis functions are as follows:

(1) Partition of unity: $\sum_{i=1}^{n} N_{i,p}(s) = 1$
(2) Compact support in the interval $[s_i, s_{i+p+1}]$
(3) Non-negativity: $N_{i,p}(s) \geqslant 0$
(4) C^{p-k} continuity where k is multiplicity of knots: if internal knots are not repeated, C^{p-1}

Generally, the smoothness of B-spline basis functions is higher than that of the conventional FEM basis functions. For a quadratic case, B-spline maintains C^1 continuity while C^0 in FEM basis function. This implies that derivative information such as stress and curvature, etc., are completely continuous in the whole spline patch. Such high smoothness has great advantages in stress calculation and analysis of shell structures which requires high smoothness.

2.2. B-spline curves and surfaces

A B-spline curve of degree p is expressed in parametric form as a linear combination of control points, $\mathbf{x}_i$, and basis functions of degree p.

$$\mathbf{C}(s) = \sum_{i=1}^{n} N_{i,p}(s)\mathbf{x}_i \tag{2}$$

B-spline surface is defined by a tensor product of basis functions with two parameters.

$$\mathbf{S}(s,t) = \sum_{i=1}^{n}\sum_{j=1}^{m} N_{i,p}(s) M_{j,q}(t)\mathbf{x}_{ij} \tag{3}$$

Here, $N_{i,p}(s)$ and $M_{j,q}(t)$ are B-spline basis functions of degree p and of degree q with respect to the parameters s and t. They are determined by their knot vectors which are given by $\mathbf{s} = [s_0, s_1, \ldots, s_{n+p}]$ and $\mathbf{t} = [t_0, t_1, \ldots, t_{m+q}]$. Then, the surface patch is defined by the interval $[s_0, s_{n+p}] \times [t_0, t_{m+q}]$ and knot span by $[s_i, s_{i+1}] \times [t_j, t_{j+1}]$ in the parametric space. In this work, two-dimensional parametric space is defined by the interval $[0,1] \times [0,1]$. The parametric space

is divided into rectangular elements by two knot vectors, $\mathbf{s} = [s_0, s_1, \ldots, s_{n+p}]$ and $\mathbf{t} = [t_0, t_1, \cdots, t_{m+q}]$.

2.3. Knot insertion and knot multiplicity

B-spline has several fundamental geometric algorithms such as knot insertion, degree elevation and knot removal, etc. (Piegl and Tiller, 1997). Among these, knot insertion is the most important and essential operation in isogeometric analysis. Knot insertion is the process of determining new control points without shape change when additional knots are inserted into a given knot vector. Simple example on knot insertion is shown in Fig. 1. Fig. 1(a) shows a quadratic B-spline curve with six control points and the knot vector, $\mathbf{s} = [0, 0, 0, 0.25, 0.5, 0.75, 1, 1, 1]$. The curve is divided into 4 elements by the knot vector. The basis functions of control points are shown in the figure. Then the curve can be refined by knot insertion without shape change as shown in Fig. 1(b). Two knots, i.e. 0.125 and 0.375, are inserted into the knot vector and two new control points are created. By inserting non-repeated knots, the number of elements increases. Knot insertion does not change the shape and the smoothness of basis functions. It is used in isogeometric analysis for refining mesh without change of the geometry. It is analogous with *h*-refinement in the conventional FEM. Fig. 1(c) illustrates the knot multiplicity operation. Two knots are repeated, i.e. 0.25 and 0.75, in the knot vector and two new control points are created while the number of elements remains the same. Note that the additional control points are located at the interface of elements. Knot multiplicity does not change the shape but changes the smoothness of the basis function for the corresponding control point. As shown in the figure, we can enforce Kronecker delta property on the additional control points by using knot multiplicity. This special property of knot multiplicity allows the introduction of sharp corners and stress discontinuity behaviors. Moreover, pointwise essential boundary conditions are easily treated by enforcing Kronecker delta property.

2.4. NURBS curve and surface

NURBS is a generalization of B-spline and it is the standard in many CAD systems at present. NURBS is weighted and rational form of B-spline. NURBS curve and surface are shown in the following equations.

$$\mathbf{C}(s) = \sum_{i=1}^{n} \frac{w_i N_{i,p}(s)}{\sum_{j=1}^{n} w_j N_{j,p}(s)} \mathbf{x}_i,$$

$$\mathbf{S}(s,t) = \sum_{i=1}^{n} \sum_{j=1}^{m} \frac{w_{ij} N_{i,p}(s) M_{j,q}(t)}{\sum_{k=1}^{n} \sum_{l=1}^{m} w_{kl} N_{k,p}(s) M_{l,q}(t)} \mathbf{x}_{ij} \tag{4}$$

Here, $\mathbf{x}_{ij}$ is the control points and w_{ij} the weight of the control point. The patch and knot spans of NURBS are defined in the same way as in B-spline. If all weights are unity, NURBS is equivalent to B-spline. Since NURBS is defined by rational basis functions derived from B-spline polynomial basis functions, it can represent circles, ellipses, cones and conics exactly which can not be exactly represented by polynomial basis functions.

2.5. T-splines

Although NURBS is the most widely used mathematical language in many CAD systems, it is highly inefficient in local refinement and patch merging. Fig. 2 illustrates the inefficient local refinement of NURBS. For refinement of a local region in interest (dashed circle in Fig. 2(a)), knots are to be propagated through the entire row or column (dashed lines in Fig. 2(b)) which contain the local region because of the tensor product nature of NURBS. The global propagation of knots causes large number of superfluous control points. Fig. 3 also illustrates an inefficient merging process of NURBS patches. To combine the NURBS patches whose interfaces are not coincident, knots are also propagated (dashed lines in the right figure of Fig. 3) through other patches. In order to overcome the inefficiencies of NURBS, T-spline was proposed by Sederberg et al. (2003, 2004). T-splines are mitigated from the strict tensor product patch concept and allow peculiar points called *T-junctions* in parametric space. The parametric space which includes the T-junctions is called *T-mesh*. The T-junctions enable T-spline surfaces to be locally refined. Without T-junctions in parametric space, T-spline surface is the same with NURBS surface. Therefore, T-spline is a generalization of NURBS and enables to reduce the number of control points dramatically. General parametric spaces of NURBS and T-spline are shown in Fig. 4. T-spline surface is written as

$$\mathbf{S}(s,t) = \sum_{i=1}^{n} \frac{w_i B_i(s,t)}{\sum_{j=1}^{n} w_j B_j(s,t)} \mathbf{x}_i \tag{5}$$

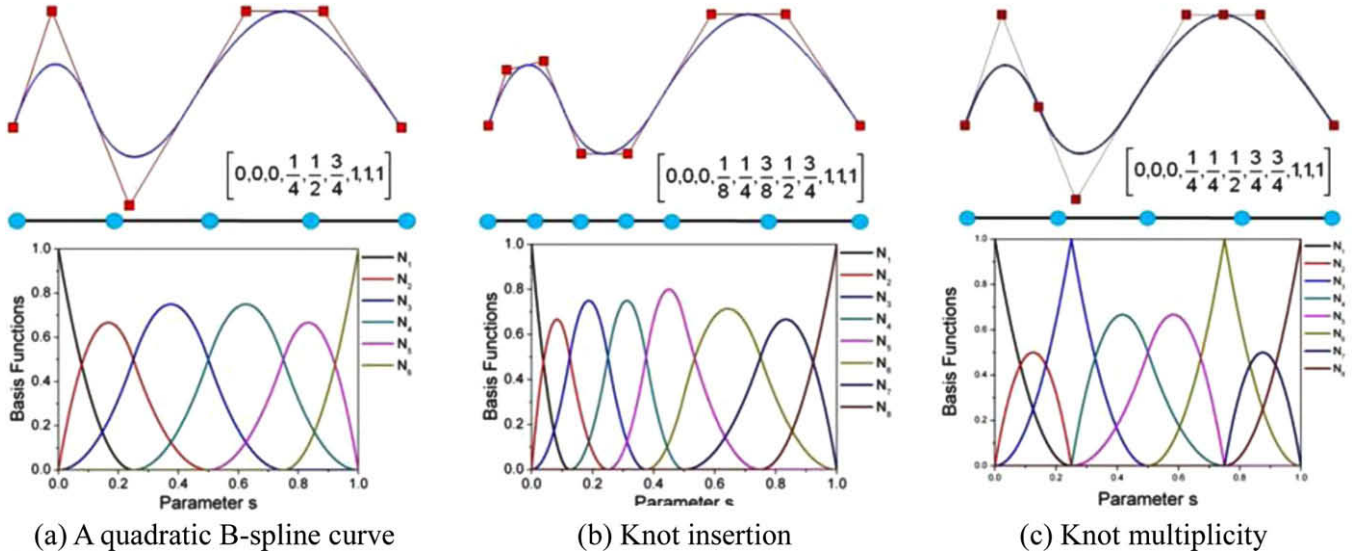

Fig. 1. Knot insertion and knot multiplicity: a quadratic B-spline curve example.

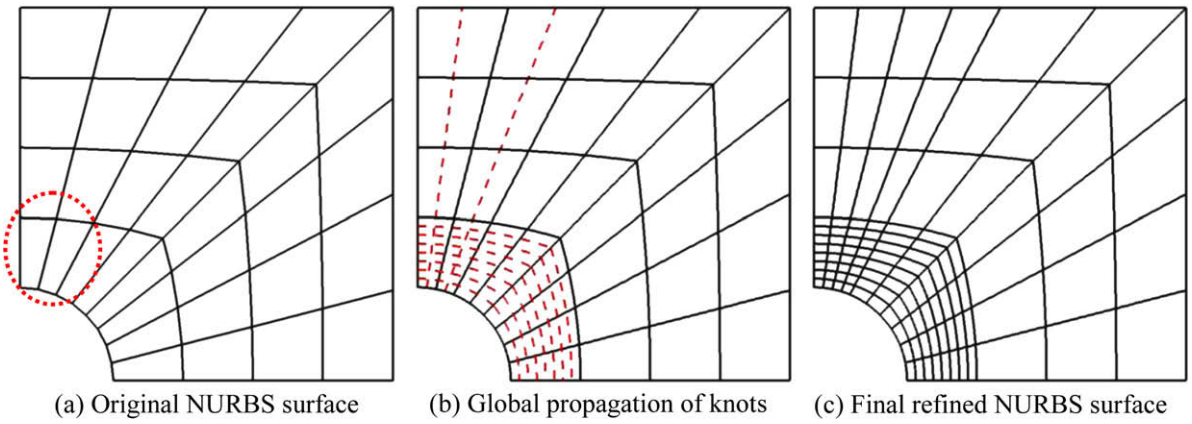

Fig. 2. Inefficiency in local refinement of NURBS surface: global propagation of knots.

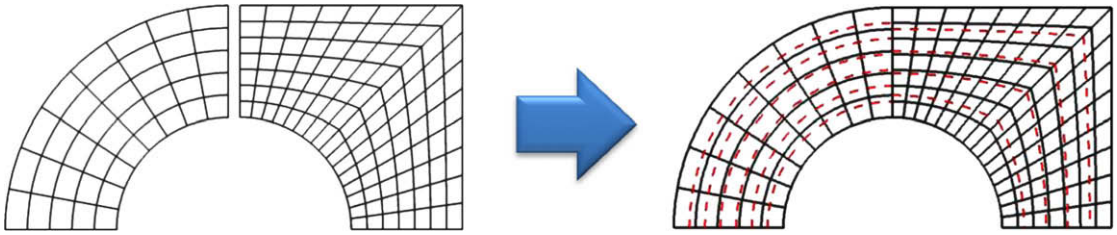

Fig. 3. Inefficient patch merging process of NURBS.

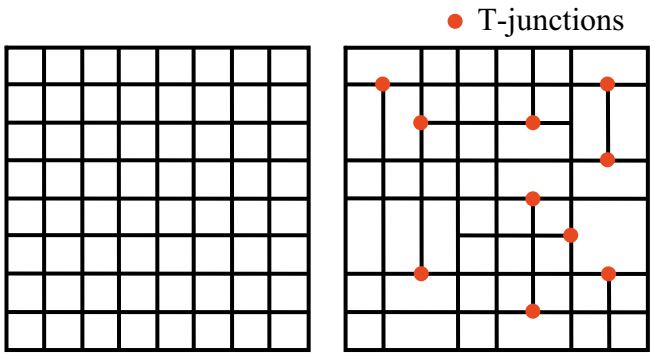

Fig. 4. The parametric domain of NURBS (left) and T-spline (right).

where $B_i(s,t)$ is defined by the product of B-spline basis functions as follow:

$$B_i(s,t) = N_{i,p}(s)N_{i,p}(t) \tag{6}$$

The B-spline basis functions, $N_{i,p}(s)$ and $N_{i,p}(t)$, are associated with the knot vectors, $\mathbf{s} = [s_i, \ldots, s_{i+p+1}]$ and $\mathbf{t} = [t_i, \ldots, t_{i+p+1}]$, respectively. Then rational form of T-spline basis function is defined as follow:

$$R_i(s,t) = \frac{w_i B_i(s,t)}{\sum_{j=1}^{n} w_j B_j(s,t)} \tag{7}$$

If there is no T-junction in parametric space, T-spline basis functions are equivalent to those of NURBS. Even though T-spline surfaces were proposed based on only cubic B-spline basis functions

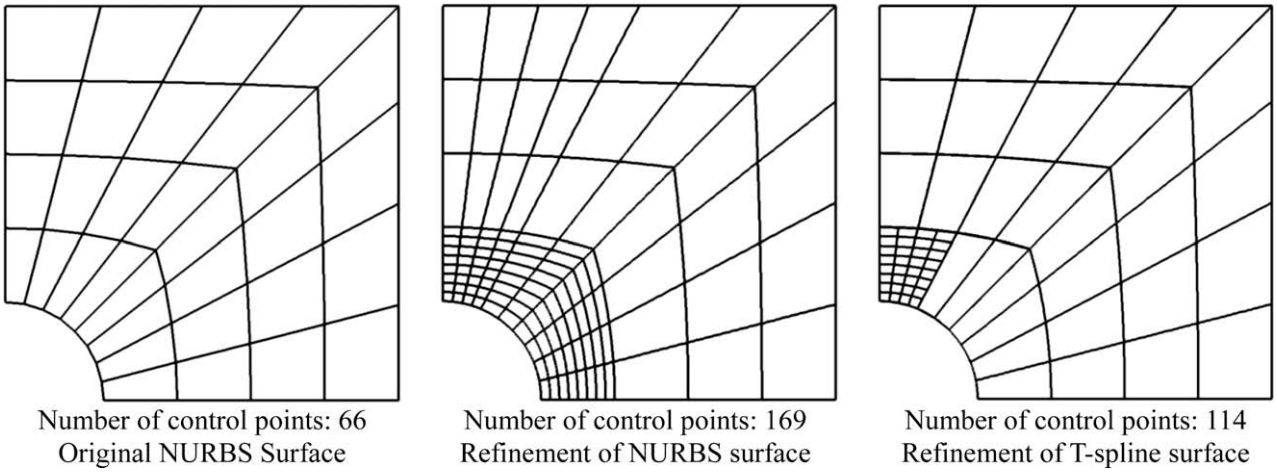

Fig. 5. Comparison of local refinement with NURBS and T-spline surfaces.

in the work of Sederberg (2003, 2004), it is also straightforward to define T-spline surface based on other degree of B-spline basis functions. More details on T-splines can be found in the literatures (Sederberg et al., 2003, 2004).

As shown in Fig. 5, efficient local refinement of T-spline is achieved without global propagation of knots. Such efficient processes prevent from creating superfluous control points. Fig. 6. illustrates efficiency of T-spline in patch merging process. The non-matching knots on the merging boundary are treated by T-junctions with T-spline while knots are globally propagated with NURBS. Consequently, the use of T-splines can resolve some instabilities in geometric modeling and reduce computational costs (time and memory) dramatically in numerical analysis.

3. Review on the conventional isogeometric analysis and trimmed surface analysis

In the present work, the analysis framework of the isogeometric analysis is used for design optimization of structures. In this section, we briefly review the isogeometric analysis and its characteristics are simply compared with those of the conventional FEM. The trimmed surface analysis which can overcome topological limitation in the conventional isogeometric analysis are also explained.

3.1. The conventional isogeometric analysis

The general procedure of the isogeometric analysis is shown in Fig. 7. At first, geometric modeling is performed in CAD systems. We can obtain the spline data for geometry information such as the coordinates of control points, weights and knots from the CAD files (*.igs, *.step). Generally, the spline data provides initial coarse mesh of the structure. Then, knot insertion is performed for fine discretization to obtain sufficient number of degree of freedoms for finite element analysis. In the figure, only global refinement of the surface is shown but, if necessary, local refinement can be also performed with T-spline. After imposing boundary conditions, finite element analysis is performed using spline basis functions.

Fig. 8 shows the quadratic finite element models of the conventional FEM and the isogeometric analysis. Less number of D.O.F. is used in the isogeometric analysis than in the conventional FEM for the same number of elements. Hence, total size of system equation is much smaller in the isogeometric analysis. In general, the isogeometric analysis yields better accuracy than the conventional FEM if the same number of D.O.F. is used for both cases. Table 1 summarizes the similar and different properties of the isogeometric analysis and the conventional FEM. Control points play the same role with nodes in FEM. Spline basis functions are used instead of polynomial basis functions to represent geometries as well as field variables.

$$\mathbf{S}(s,t) = \sum_{i=1}^{n} R_i(s,t)\mathbf{x}_i, \quad \mathbf{u} = \mathbf{R}\mathbf{d} \tag{8}$$

Entities in the local displacement vector $\mathbf{d}$ are the displacement at control points. Structural responses are determined at the control points by solving system equation and the overall response is represented by the responses at control points and the spline basis functions. Knot spans construct finite elements in parametric space. Geometries are exactly represented with spline basis functions in the isogeometric analysis while approximated with polynomial basis functions in the conventional FEM.

3.2. The trimmed surface analysis

Main limitation of the conventional isogeometric analysis is that analysis models should be composed of tensor-product spline patches. Thus, it is very difficult to treat topologically complex models with the conventional isogeometric analysis. Although such complex models can be easily expressed by simple trimming operation in computer graphics, they should be divided into several quadrilateral patches for the isogeometric analysis and these patches should be fitted together with seamless interfaces. Therefore, additional huge modeling effort for analysis is required.

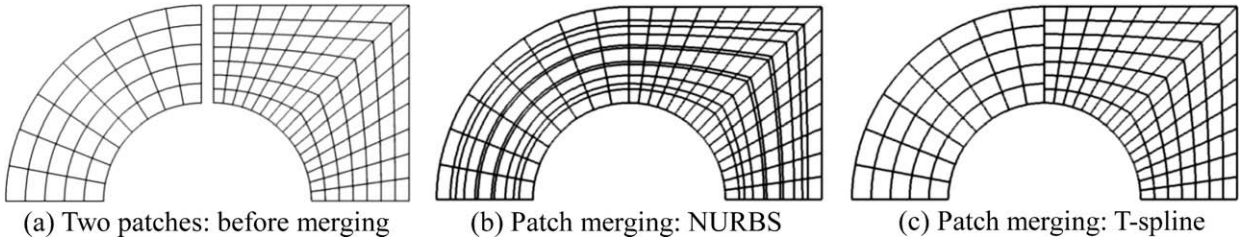

Fig. 6. Comparison of patch merging with NURBS and T-spline surfaces.

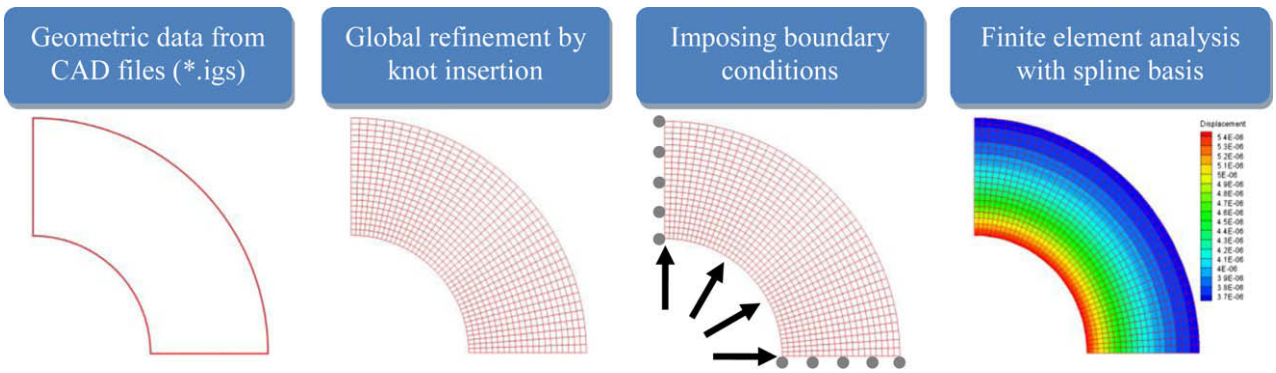

Fig. 7. The procedure of spline FEM.

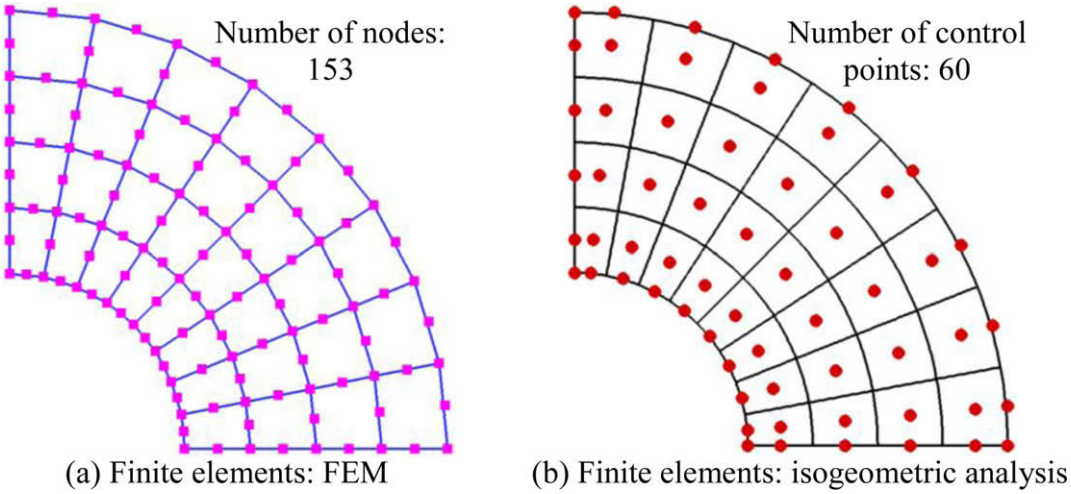

Fig. 8. A quadratic finite element models of the conventional FEM and isogeometric analysis.

Table 1
Comparison of isogeometric analysis and the conventional FEM.

Conventional FEM	Isogeometric analysis
Nodal points	Control points
Elements	Knot spans
Polynomial basis function	Spline basis function (polynomial or rational)
Approximated geometry	Exact geometry

Trimmed surface analysis was proposed by Kim et al. (2009) to overcome the topological limitation in isogeometric analysis. Main idea of the trimmed surface analysis is the direct use of trimming information such as an untrimmed surface and a set of trimming curves which are provided from CAD files. In the conventional isogeometric analysis, the parametric space of an analysis model is divided into rectangular elements by bidirectional knot spans. Thus, numerical integration of those elements is straightforward. However, if trimming curves are introduced in a surface, the elements which are trimmed out by trimming curves are no longer rectangular. The key issue in the trimmed surface analysis is the exact integration of the trimmed elements of arbitrary shape.

Let us consider a trimmed surface shown in Fig. 9(a). For the trimmed surface, CAD provides the untrimmed surface, four trimming curves in physical space and those in parametric space. Fig. 9(b) illustrates the parametric space of the untrimmed surface. Then, elements are classified by three kinds as shown in Fig. 9(c). Untrimmed elements inside analysis model (blue) are integrated by Gauss quadrature rule for rectangle and untrimmed elements outside analysis model (red) are excluded from analysis. Since the trimmed elements (green) are not quadrilateral, they should be divided into sub-integration cells. The trimmed elements can be also classified by three kinds based on the number of element vertices excluded from analysis model (red points) as shown in Fig. 10.[1] In case of complicated trimmed elements which do not match to the three kinds, those elements are divided by quadtree refinement until the quadtreely refined cells satisfy one of the three trimmed cases. The trimmed elements are decomposed right triangular integration cells and curved ones for numerical integration. The curved triangular integration cells have curved boundary which is a part of trimming spline curve. The right triangular cells are integrated by Gauss quadrature rule for triangles. For exact numerical integration of the curved triangular cells, the modified integration scheme inspired from NURBS-enhanced integration scheme (Sevilla et al., 2008) was proposed in the trimmed surface analysis (Kim et al., 2009). Note that integration cell decomposition is performed in the parametric space of the untrimmed surface since the parametric space is simpler than the physical one.

The element stiffness matrix is given by

$$\mathbf{k_e} = \int \mathbf{B^T D B} d\Omega = \int_{-1}^{1}\int_{-1}^{1} \mathbf{B^T D B} |\mathbf{J}| d\xi d\eta = \sum_{k=1}^{NINT} \mathbf{B}_k^{\mathbf{T}} \mathbf{D} \mathbf{B}_k |\mathbf{J}_k| W_k \tag{9}$$

where **B** is strain-displacement matrix, **D** the constitutive matrix, **J** the Jacobian, $|\mathbf{J}|$ the determinant of Jacobian and W the weight at each integration points. *NINT* is the number of Gauss quadrature. The matrix **B** is expressed in the following discrete form.

$$\mathbf{B} = \mathbf{M\Gamma G}$$

$$\mathbf{M} = \begin{bmatrix} 1 & 0 & 0 & 0 \\ 0 & 0 & 0 & 1 \\ 0 & 1 & 1 & 0 \end{bmatrix}, \quad \mathbf{\Gamma} = \begin{bmatrix} \mathbf{J_S}^{-1} & 0 \\ 0 & \mathbf{J_S}^{-1} \end{bmatrix}, \quad \mathbf{G} = \begin{bmatrix} R_{1,s} & 0 & R_{2,s} & 0 & \cdots & R_{n,s} & 0 \\ R_{1,t} & 0 & R_{2,t} & 0 & \cdots & R_{n,t} & 0 \\ 0 & R_{1,s} & 0 & R_{2,s} & \cdots & 0 & R_{n,s} \\ 0 & R_{1,t} & 0 & R_{2,t} & \cdots & 0 & R_{n,t} \end{bmatrix} \tag{10}$$

$\mathbf{J_S}$ is the transformation mapping from the parametric space to the physical one and is written as

$$\mathbf{J_S} = \begin{bmatrix} x_{,s} & y_{,s} \\ x_{,t} & y_{,t} \end{bmatrix} = \begin{bmatrix} \sum_{i=1}^{n} R_{i,s} x_i & \sum_{i=1}^{n} R_{i,s} y_i \\ \sum_{i=1}^{n} R_{i,t} x_i & \sum_{i=1}^{n} R_{i,t} y_i \end{bmatrix} \tag{11}$$

B and $\mathbf{J_S}$ are in the same form regardless of the type of integration cells while Jacobian **J** is different according to the integration cells.

In rectangular integration cells, Jacobian **J** and its determinant are calculated in the same way with the conventional isogeometric analysis. Jacobian of the element which is defined by two knot spans $[s_i, s_{i+1}] \times [t_j, t_{j+1}]$ is written as

$$\mathbf{J} = \mathbf{J_R J_S} = \begin{bmatrix} \frac{s_{i+1}-s_i}{2} & 0 \\ 0 & \frac{t_{j+1}-t_j}{2} \end{bmatrix} \begin{bmatrix} \sum_i R_{i,s} x_i & \sum_i R_{i,s} y_i \\ \sum_i R_{i,t} x_i & \sum_i R_{i,t} y_i \end{bmatrix}, \quad |\mathbf{J}| = |\mathbf{J_R}||\mathbf{J_S}| \tag{12}$$

In case of right triangular integration cells, a linear transformation **R** is required for integration as shown in Fig. 11. The transformation **R** is simply expressed by linear triangular shape functions in FEM.

[1] For interpretation of references to color in Figs. 9 and 10, the reader is referred to the web version of this article.

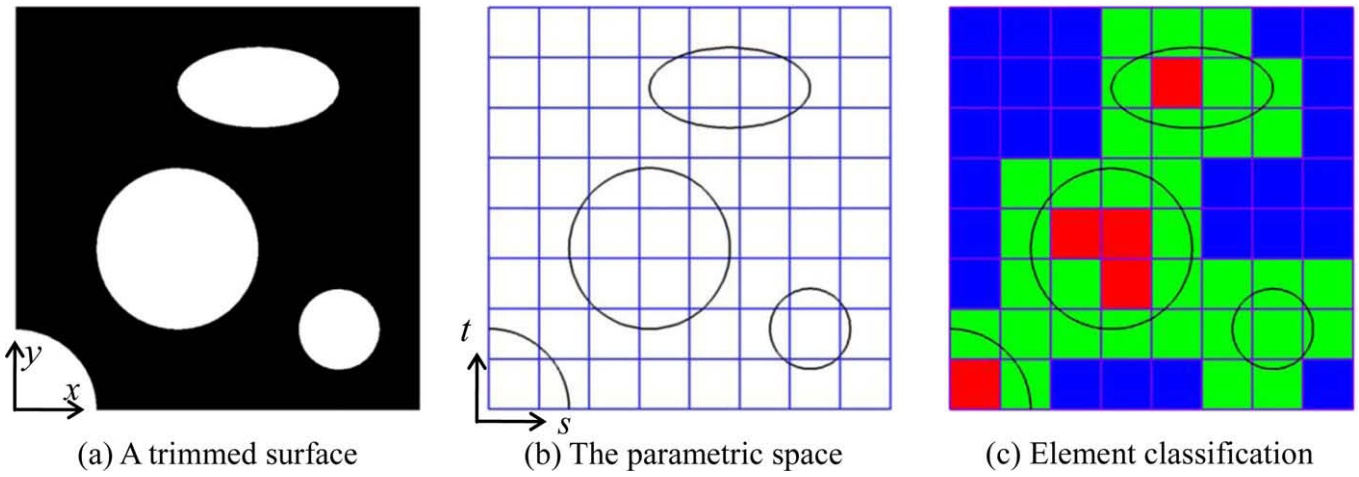

Fig. 9. A trimmed surface and classification of its elements.

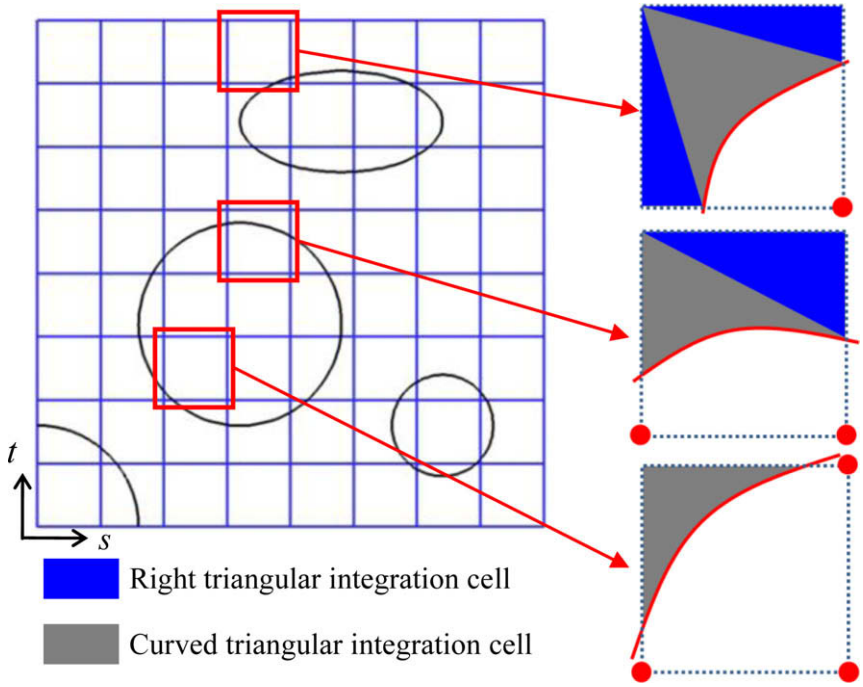

Fig. 10. Three kinds of trimmed elements and integration cell decomposition.

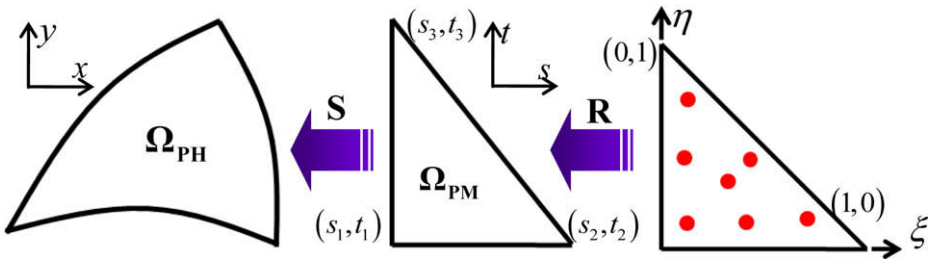

Fig. 11. Transformations in right triangular integration cells.

$$\mathbf{R}:\{\xi,\eta\}\rightarrow\{s,t\}\quad\begin{cases}s=(1-\xi-\eta)s_1+(\xi)s_2+(\eta)s_3\\ t=(1-\xi-\eta)t_1+(\xi)t_2+(\eta)t_3\end{cases}\tag{13}$$

Two vertices of right triangular integration cells, (s_1,t_1) and (s_2,t_2), are coincident with the vertices of the trimmed rectangular elements and the other vertex (s_3,t_3) which lies on a trimming curve is intersection of the trimmed element edge and the trimming curve as shown in Fig. 12. The coordinates of the intersection and its corresponding parameter of the trimming curve are determined by simple point inversion scheme (Piegl and Tiller, 1997). Then, Jacobian **J** in right triangular cells is written as

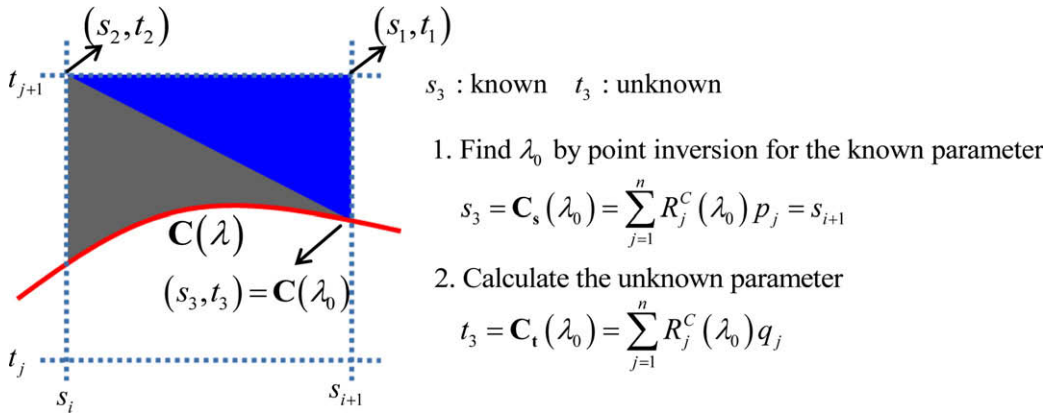

Fig. 12. Finding intersection and its corresponding parameter of the trimming curve in a right triangular integration cell.

$$\mathbf{J}=\mathbf{J_R}\mathbf{J_S}=\begin{bmatrix}-s_1+s_2 & -t_1+t_2\\ -s_1+s_3 & -t_1+t_3\end{bmatrix}\begin{bmatrix}\sum_i R_{i,s}x_i & \sum_i R_{i,s}y_i\\ \sum_i R_{i,t}x_i & \sum_i R_{i,t}y_i\end{bmatrix},\quad |\mathbf{J}|=\frac{1}{2}|\mathbf{J_R}||\mathbf{J_S}| \tag{14}$$

Fig. 13 illustrates the linear transformations from Gauss quadrature integration cell to a physical space for numerical integration of a curved triangular integration cell. $\mathbf{\Omega_{PH}}$ is a triangular cell in physical space and $\mathbf{\Omega_{PM}}$ in parametric space. In a curved triangular cell, a vertex (s_1,t_1) is coincident with one of the trimmed rectangular element vertices. The other two vertices (s_2,t_2) and (s_3,t_3) are intersections which lie on the trimming curve. The intersections and their corresponding parameters of the trimming curve, λ_1 and λ_2, are determined by the point inversion as shown in Fig. 14.

The transformations **P**, **Q**, and **R** are written as follows (Kim et al., 2009):

$$\mathbf{P}:\{\xi,\eta\}\rightarrow\{\lambda,\varsigma\}\quad\begin{cases}\lambda=\frac{\xi}{2}(\lambda_2-\lambda_1)+\frac{1}{2}(\lambda_2+\lambda_1)\\ \varsigma=\frac{\eta}{2}+\frac{1}{2}\end{cases} \tag{15}$$

$$\mathbf{Q}:\{\lambda,\varsigma\}\rightarrow\{\alpha,\beta\}\quad\begin{cases}\alpha=\phi_\alpha(\lambda)(1-\varsigma)\\ \beta=\phi_\beta(\lambda)(1-\varsigma)+\varsigma\end{cases} \tag{16}$$

$$\mathbf{R}:\{\alpha,\beta\}\rightarrow\{s,t\}\quad\begin{cases}s=(\beta)s_1+(1-\alpha-\beta)s_2+(\alpha)s_3\\ t=(\beta)t_1+(1-\alpha-\beta)t_2+(\alpha)t_3\end{cases}$$
$$\Rightarrow\begin{pmatrix}s\\ t\end{pmatrix}=\begin{bmatrix}-s_2+s_3 & s_1-s_2\\ -t_2+t_3 & t_1-t_2\end{bmatrix}\begin{pmatrix}\alpha\\ \beta\end{pmatrix}+\begin{pmatrix}s_2\\ t_2\end{pmatrix} \tag{17}$$
$$\Rightarrow\begin{pmatrix}s\\ t\end{pmatrix}=\mathbf{A}\begin{pmatrix}\alpha\\ \beta\end{pmatrix}+\mathbf{B}$$

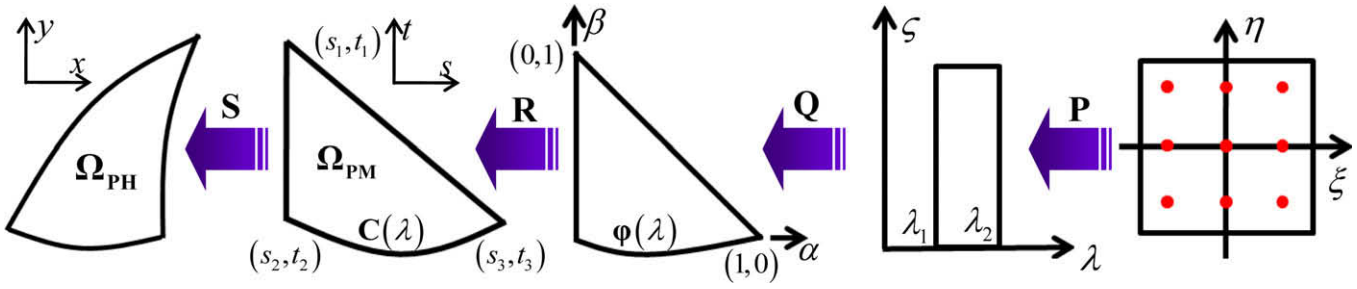

Fig. 13. Transformations in curved triangular integration cells.

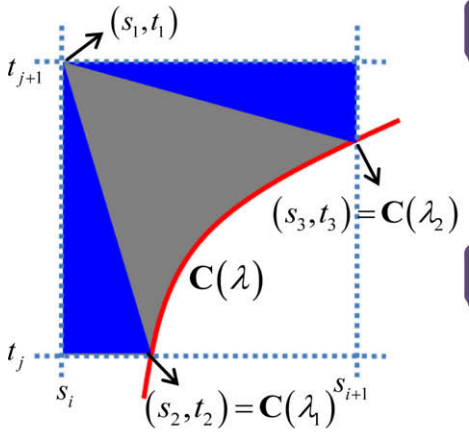

Vertex 2 s_2 : unknown t_2 : known

1. Find λ_1 from $t_2=\mathbf{C}_t(\lambda_1)=\sum_{k=1}^{n}R_k^C(\lambda_1)q_k=t_j$

2. $s_2=\mathbf{C}_s(\lambda_1)=\sum_{k=1}^{n}R_k^C(\lambda_1)p_k$

Vertex 3 s_3 : known t_3 : unknown

1. Find λ_2 from $s_3=\mathbf{C}_s(\lambda_2)=\sum_{k=1}^{n}R_k^C(\lambda_2)p_k=s_{i+1}$

2. $t_3=\mathbf{C}_t(\lambda_2)=\sum_{k=1}^{n}R_k^C(\lambda_2)q_k$

Fig. 14. Finding intersections and their corresponding parameters of the trimming curve in a curved triangular integration cell.

The transformed trimming curve in $\alpha\beta$-coordinate $\boldsymbol{\varphi}(\lambda) = [\phi_\alpha(\lambda)\ \phi_\beta(\lambda)]^T$ can be derived from the inverse transformation $\mathbf{R}^{-1}$. Thus it can be rewritten as

$$\boldsymbol{\varphi}(\lambda) = \mathbf{R}^{-1} \circ \mathbf{C}(\lambda) = \mathbf{A}^{-1}(\mathbf{C}(\lambda) - \mathbf{B}) \tag{18}$$

Then, Jacobian $\mathbf{J}$ in curved triangular integration cells is given by

$$\mathbf{J} = \mathbf{J_P}\mathbf{J_Q}\mathbf{J_R}\mathbf{J_S} = \begin{bmatrix} \frac{\partial\lambda}{\partial\xi} & \frac{\partial\zeta}{\partial\xi} \\ \frac{\partial\lambda}{\partial\eta} & \frac{\partial\zeta}{\partial\eta} \end{bmatrix} \begin{bmatrix} \frac{\partial\alpha}{\partial\lambda} & \frac{\partial\beta}{\partial\lambda} \\ \frac{\partial\alpha}{\partial\zeta} & \frac{\partial\beta}{\partial\zeta} \end{bmatrix} \begin{bmatrix} \frac{\partial s}{\partial\alpha} & \frac{\partial t}{\partial\alpha} \\ \frac{\partial s}{\partial\beta} & \frac{\partial t}{\partial\beta} \end{bmatrix} \begin{bmatrix} \frac{\partial x}{\partial s} & \frac{\partial y}{\partial s} \\ \frac{\partial x}{\partial t} & \frac{\partial y}{\partial t} \end{bmatrix}, \quad |\mathbf{J}| = |\mathbf{J_P}||\mathbf{J_Q}||\mathbf{J_R}||\mathbf{J_S}| \tag{19}$$

where

$$\mathbf{J_P} = \begin{bmatrix} \frac{\partial\lambda}{\partial\xi} & \frac{\partial\zeta}{\partial\xi} \\ \frac{\partial\lambda}{\partial\eta} & \frac{\partial\zeta}{\partial\eta} \end{bmatrix} = \begin{bmatrix} \frac{\lambda_2-\lambda_1}{2} & 0 \\ 0 & \frac{1}{2} \end{bmatrix}, \quad \mathbf{J_Q} = \begin{bmatrix} \frac{\partial\alpha}{\partial\lambda} & \frac{\partial\beta}{\partial\lambda} \\ \frac{\partial\alpha}{\partial\zeta} & \frac{\partial\beta}{\partial\zeta} \end{bmatrix} = \begin{bmatrix} \frac{\partial\phi_\alpha(\lambda)}{\partial\lambda}(1-\varsigma) & \frac{\partial\phi_\beta(\lambda)}{\partial\lambda}(1-\varsigma) \\ -\phi_\alpha(\lambda) & -\phi_\beta(\lambda)+1 \end{bmatrix} \quad \text{and}$$

$$\mathbf{J_R} = \begin{bmatrix} \frac{\partial s}{\partial\alpha} & \frac{\partial t}{\partial\alpha} \\ \frac{\partial s}{\partial\beta} & \frac{\partial t}{\partial\beta} \end{bmatrix} = \begin{bmatrix} -s_2+s_3 & -t_2+t_3 \\ s_1-s_2 & t_1-t_2 \end{bmatrix}.$$

By using Eq. (17), $\frac{\partial\phi_\alpha(\lambda)}{\partial\lambda}$ and $\frac{\partial\phi_\beta(\lambda)}{\partial\lambda}$ can be calculated as follow.

$$\begin{pmatrix} \frac{\partial\phi_\alpha(\lambda)}{\partial\lambda} \\ \frac{\partial\phi_\beta(\lambda)}{\partial\lambda} \end{pmatrix} = \frac{\partial\left(\mathbf{A}^{-1}(C(\lambda)-\mathbf{B})\right)}{\partial\lambda} = \mathbf{A}^{-1}\left(\frac{\partial C(\lambda)}{\partial\lambda}\right) \tag{20}$$

Fig. 15 shows decomposed integration cells and integration points in them. Integration points in curved triangular integration cells are well distributed near the curved boundaries by the proposed transformations shown in Fig. 14. Consequently, the stiffness matrix of a curved triangular integration cell can be calculated by applying Eq. (19) to Eq. (9).

4. Shape sensitivity analysis with trimmed surface analysis

In the present work, the coordinates of the control points that represent the boundaries of a surface are chosen as design variables. Then general shape optimization can be written as follows:

$$\begin{aligned} &\text{Minimize} \quad \Psi(\mathbf{x},\mathbf{u}(\mathbf{x})) \\ &\text{subject to} \quad h_j(\mathbf{x},\mathbf{u}(\mathbf{x})) = 0 \quad j = 1,\ldots,\text{Number of equality constraint} \\ &\qquad\qquad g_k(\mathbf{x},\mathbf{u}(\mathbf{x})) \leqslant 0 \quad k = 1,\ldots,\text{Number of inequality constraint} \\ &\qquad\qquad \underline{x}_i \leqslant x_i \leqslant \bar{x}_i \quad i = 1,\ldots,\text{Number of design variables} \end{aligned} \tag{21}$$

where Ψ is the objective function and $\mathbf{x}$ the design variable and $\mathbf{u}(\mathbf{x})$ the field variable, e.g. the displacements. x_i and $\bar{x}_i$ are the lower and upper bound(side constraint) of the design variables, respectively. The method of moving asymptotes (MMA) (Svanberg, 1987) is employed as an optimizer. In order to use the gradient-based algorithm, an accurate calculation of sensitivity is essential. In this section, analytic sensitivities on compliance and maximum stress are derived in discrete manner and their accuracy is verified.

4.1. Analytic sensitivity calculation

When compliance is chosen as an objective function, its sensitivities with respect to the design variables, i.e. the coordinates of control points of the surface, can be derived as follows.

Discrete form of compliance is written as

$$\Psi(\mathbf{x},\mathbf{u}(\mathbf{x})) = \mathbf{F}^T\mathbf{u} \tag{22}$$

where $\mathbf{F}$ is the force vector in linear system equation and $\mathbf{u}$ the displacement vector. In case of a design independent concentrated force, the sensitivities of compliance with respect to design variables written as follows since derivative of force vector is eliminated.

$$\frac{\partial\Psi}{\partial\mathbf{x}} = \mathbf{F}^T\frac{\partial\mathbf{u}}{\partial\mathbf{x}} = -\mathbf{F}^T\mathbf{K}^{-1}\frac{\partial\mathbf{K}}{\partial\mathbf{x}}\mathbf{u} = -\mathbf{u}^T\frac{\partial\mathbf{K}}{\partial\mathbf{x}}\mathbf{u} \tag{23}$$

The element stiffness matrix $\mathbf{k_e}$ shown in Eq. (9) is assembled to form the stiffness matrix. Then, the derivative of the element stiffness matrix with respect to the design variable is

$$\frac{\partial\mathbf{k_e}}{\partial\mathbf{x}} = \sum_{k=1}^{NINT}\left[\frac{\partial\mathbf{B}_k^T}{\partial\mathbf{x}}\mathbf{D}\mathbf{B}_k|\mathbf{J}_k|W_k + \mathbf{B}_k^T\mathbf{D}\frac{\partial\mathbf{B}_k}{\partial\mathbf{x}}|\mathbf{J}_k|W_k + \mathbf{B}_k^T\mathbf{D}\mathbf{B}_k\frac{\partial|\mathbf{J}_k|}{\partial\mathbf{x}}W_k\right] \tag{24}$$

The derivative of $\mathbf{B}$ is written as follow:

$$\frac{\partial\mathbf{B}}{\partial\mathbf{x}} = \mathbf{M}\frac{\partial\boldsymbol{\Gamma}}{\partial\mathbf{x}}\mathbf{G} \text{ where } \frac{\partial\boldsymbol{\Gamma}}{\partial\mathbf{x}} = \begin{bmatrix} \frac{\partial\mathbf{J_S}^{-1}}{\partial\mathbf{x}} & 0 \\ 0 & \frac{\partial\mathbf{J_S}^{-1}}{\partial\mathbf{x}} \end{bmatrix} \text{ and } \frac{\partial\mathbf{J_S}^{-1}}{\partial\mathbf{x}} = -\mathbf{J_S}^{-1}\frac{\partial\mathbf{J_S}}{\partial\mathbf{x}}\mathbf{J_S}^{-1} \tag{25}$$

As explained in the previous section, the transformation relations are different according to the type of integration cell. Among those transformations, only $\mathbf{J_S}$ is dependent on the coordinates of surface control points while others are independent. Thus, the derivative of $|\mathbf{J}|$ is expressed in terms of that of $|\mathbf{J_S}|$.

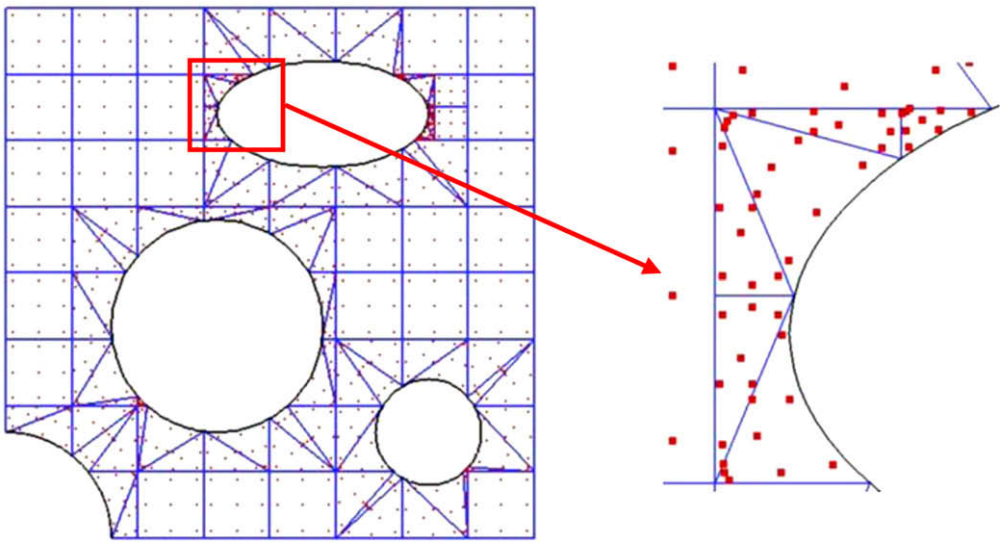

Fig. 15. Integration cell decomposition and integration points in the cells.

$$\frac{\partial|\mathbf{J}|}{\partial \mathbf{x}} = |\mathbf{J_R}|\frac{\partial|\mathbf{J_S}|}{\partial \mathbf{x}}: \text{ rectangular and right triangular cells}$$
$$\frac{\partial|\mathbf{J}|}{\partial \mathbf{x}} = |\mathbf{J_P}||\mathbf{J_Q}||\mathbf{J_R}|\frac{\partial|\mathbf{J_S}|}{\partial \mathbf{x}}: \text{ curved triangular cells} \quad (26)$$

The sensitivity of element stiffness matrix can be evaluated by applying Eqs. (25) and (26) to Eq. (24). Then, the sensitivity of the compliance can be obtained by summing up the sensitivities of the compliance within the elements which are included in the compact support of the basis function of the design variable.

$$\frac{\partial \Psi}{\partial \mathbf{x}} = -\mathbf{u}^{\mathbf{T}}\frac{\partial \mathbf{K}}{\partial \mathbf{x}}\mathbf{u} = -\sum_{i=1}^{NECS}\mathbf{u}^{\mathbf{T}}\frac{\partial \mathbf{k}_i}{\partial \mathbf{x}}\mathbf{u} \quad (27)$$

NECS is the number of elements in the compact support of a certain design variable.

Under certain circumstances, minimizing the maximum stress of a structure is often desired in structural shape optimization. In the present work, the maximum von-Mises stress described below is considered as a stress measure.

$$\sigma_{VON} = \left[\frac{\sigma_1^2+\sigma_2^2+(\sigma_1-\sigma_2)^2+6\sigma_{12}^2}{2}\right]^{1/2} = \left[\frac{\tilde{\boldsymbol{\sigma}}^{\mathbf{T}}\tilde{\boldsymbol{\sigma}}}{2}\right]^{1/2} \quad (28)$$

where $\tilde{\boldsymbol{\sigma}} = [\sigma_1 \quad \sigma_2 \quad \sigma_1-\sigma_2 \quad \sqrt{6}\sigma_{12}]^{\mathbf{T}}$.

Then, the derivative of von-Mises stress with respect to a coordinate of control point is as follow.

$$\frac{d\sigma_{VON}}{d\mathbf{x}} = \frac{1}{2\sigma_{VON}}\tilde{\boldsymbol{\sigma}}^{\mathbf{T}}\frac{d\tilde{\boldsymbol{\sigma}}}{d\mathbf{x}} \quad (29)$$

To compute the above equation, the derivatives of stress components should be derived. The local stress vector at the maximum stress point can be written in discrete form as

$$\boldsymbol{\sigma}_{MAX} = \begin{bmatrix}\sigma_1\\ \sigma_2\\ \sigma_3\end{bmatrix} = \mathbf{DBd} = \mathbf{DBAu}. \quad (30)$$

Here, **d** is the local displacement vector of the control points concerned with the maximum stress point while **u** the global one. **A** is a matrix which transforms the global displacement vector to the local one. Since the maximum stress is a localized performance whereas compliance represents global behavior, the transformation matrix **A** is desired to represent the maximum stress with respect to the global components. **A** has the value 1 at the degree of freedom corresponding to the local displacement vector and zeros at other places. Then, the sensitivity of the local behavior can be derived as follow:

$$\frac{\mathrm{d}\boldsymbol{\sigma}}{\mathrm{d}\mathbf{x}} = \frac{\partial \boldsymbol{\sigma}}{\partial \mathbf{x}} + \frac{\partial \boldsymbol{\sigma}}{\partial \mathbf{u}}\frac{\partial \mathbf{u}}{\partial \mathbf{x}} = \mathbf{D}\frac{\partial \mathbf{B}}{\partial \mathbf{x}}\mathbf{Au} + \mathbf{DBA}\frac{\partial \mathbf{u}}{\partial \mathbf{x}}$$
$$= \mathbf{D}\frac{\partial \mathbf{B}}{\partial \mathbf{x}}\mathbf{Au} - \mathbf{DBAK}^{-1}\frac{\partial \mathbf{K}}{\partial \mathbf{x}}\mathbf{u} = \mathbf{D}\frac{\partial \mathbf{B}}{\partial \mathbf{x}}\mathbf{Au} - \mathbf{v}^{T}\frac{\partial \mathbf{K}}{\partial \mathbf{x}}\mathbf{u} \quad (31)$$

where **v** is the solution of the following adjoint equation.

$$\mathbf{Kv} = (\mathbf{DBA})^{\mathbf{T}} \quad (32)$$

4.2. Verification of sensitivity analysis

The derived analytic sensitivities are verified by comparing with those obtained from finite difference method (FDM). The verification model shown in Fig. 16(a) is a cantilever beam that is subjected to the concentrated force along the vertical direction at the bottom right corner. The finite element model and its control points are shown in Fig. 16(b). Stress contour resulting from isogeometric analysis is also shown in Fig. 16(c). In Table 2, sensitivities of compliance and the maximum stress with respect to the coordinates of the six chosen control points in Fig. 16(b) are compared with those of FDM. For FDM calculation, 0.1% perturbation of the design variables, that is, 0.2 mm for the horizontal coordinates and 0.12 mm for the vertical coordinates, is given. As shown in Table 2, analytic sensitivities are in good agreement with those from FDM calculation.

5. Shape optimization results

The isogeometric analysis is applied to shape optimization problems. In this work, 2D and simple shell problems are treated.

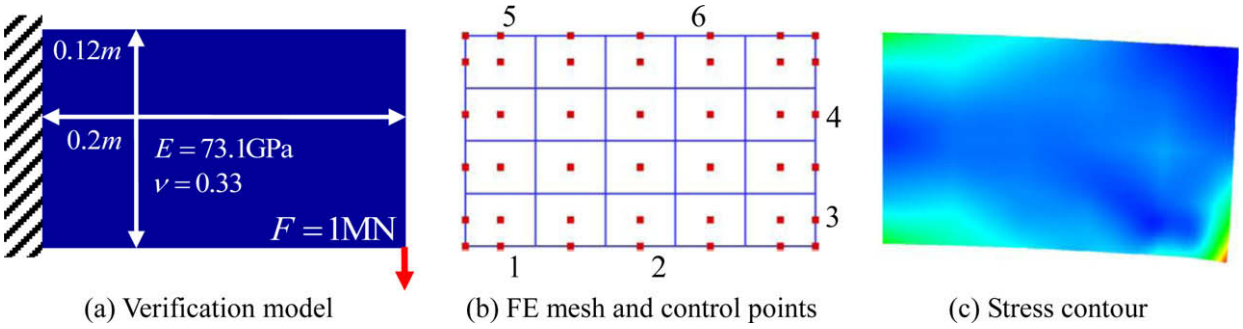

Fig. 16. Verification model for sensitivity analysis.

Table 2
Verification of sensitivity analysis: the compliance and the maximum stress.

Design variables	Compliance			Maximum stress		
	Sensitivity analysis	FDM	Error (%)	Sensitivity analysis	FDM	Error (%)
1	1.947E+03	1.952E+03	−0.215	6.915E+06	6.914E+06	0.021
2	1.065E+03	1.068E+03	−0.271	4.386E+07	4.376E+07	0.237
3	−2.862E+03	−2.843E+03	0.673	2.652E+09	2.634E+09	0.705
4	−1.424E+02	−1.418E+02	0.480	−5.298E+07	−5.259E+07	0.736
5	−1.960E+03	−1.956E+03	0.214	1.400E+07	1.400E+07	−0.018
6	−2.591E+02	−2.583E+02	0.302	−3.339E+05	−3.318E+05	0.605

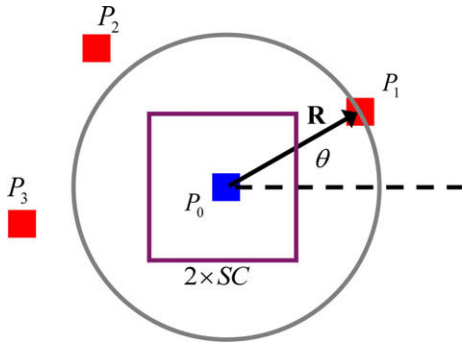

Fig. 17. Determination of the side constraints.

Two dimensional examples are assumed under plane stress condition.

The side constraints of the design variables shown in Eq. (21) are crucial for success of shape optimization. In order to prevent entanglement of the control points, strict side constraints of the design variables are assigned during optimization process. Fig. 17 illustrates how to determine the side constraints of a certain design variable (P_0). For the design variables, we find the closest control points. Then the minimum distance R can be determined and the side constraint of the design variable is defined in following equation.

$$SC = 0.5R\max[\sin\theta, \cos\theta], \quad \underline{x}_i = x_i - SC, \quad \bar{x}_i = x_i + SC \tag{33}$$

In all examples, the following convergence criterion is employed.

$$\varepsilon = \frac{\Psi_{current} - \Psi_{previous}}{\Psi_{previous}} \leqslant 10^{-6} \tag{34}$$

5.1. A fillet design: minimization of the maximum stress

The first problem is a fillet design and the problem definition is shown in Fig. 18. The quarter model of the fillet with symmetric boundary conditions and a uniformly distributed force on the right side is shown. The material properties used in this example are $E = 73.1$ GPa and $v = 0.33$. The fillet model is constructed by three B-spline surface patches which have the same knot vector along the vertical direction. As shown in Fig. 18(a), the top edge of the middle patch is the design boundary. In this example, the vertical coordinates of the control points (Fig. 18(b)) which represent the design boundary, are design variables. The objective of this problem is to minimize the maximum stress with volume reduction. Fig. 19 shows the stress contours of the initial and the final design. The final FE mesh and distribution of the control points are also shown in the figure. The concentrated initial stress is well distributed in the final design with 37% lower maximum stress and 3.3% less volume.

Note that the interior control points of the middle patch have moved during optimization process. Their movements were determined by boundary displacement method (Choi and Kim, 2005). More details on boundary displacement method will be explained in the third example.

5.2. A hole design in a finite plate: minimization of the maximum stress

Another traditional shape optimization problem is treated. Problem definition is shown in Fig. 20. Due to symmetry, the quarter model with symmetric boundary conditions and a uniformly distributed force on the right side is used in shape optimization. The boundary that represents hole shape is the design boundary while other boundaries are kept unchanged. The initial finite element model and distribution of control points of the NURBS surface are shown in Fig. 20(b). The design model is represented by a single NURBS surface patch with the two knot vectors, $\mathbf{s} = [0, 0, 0, 0.146, 0.5, 0.854, 1, 1, 1]$ and $\mathbf{t} = [0, 0, 0, 0.25, 0.5, 0.75, 1, 1, 1]$. To represent sharp corner at the upper right, two control points are overlapped each other at the coordinate of $(0.4, 0.4)$. The knot vector along $\mathbf{t}$-direction consists of uniformly spaced knots while that along $\mathbf{s}$-direction consists of non-uniform knots. If uniform knots are employed in the knot vector along $\mathbf{s}$-direction in this model, elements

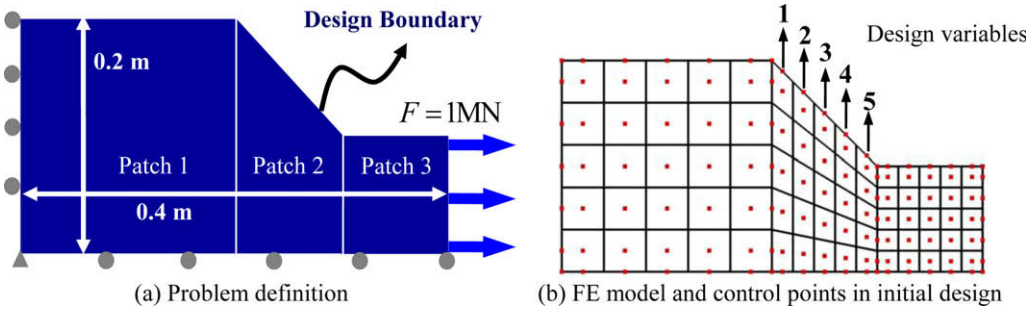

Fig. 18. Problem definition of the fillet design problem.

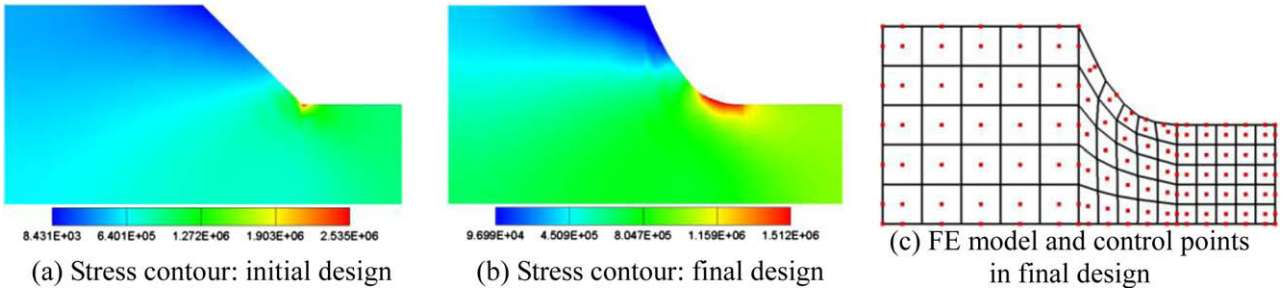

Fig. 19. Final design result: fillet design problem.

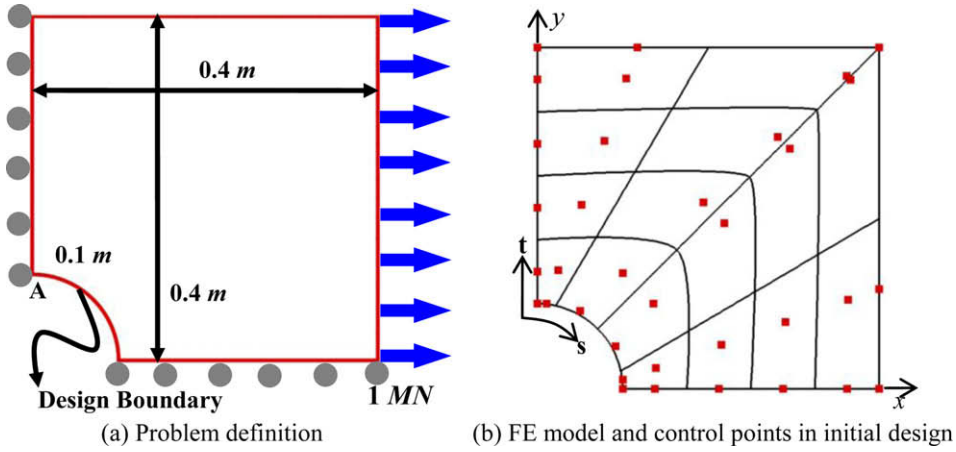

Fig. 20. Problem definition of the hole design in a finite plate.

may be highly distorted (Hughes et al., 2005). To avoid such element distortion, the knot values used in the knot vector along **s**-direction, i.e. 0.146 and 0.854, are inversely determined by the point inversion scheme (Piegl and Tiller, 1997). The NURBS surface is divided into 16 elements by the knot vectors and has 36 control points. The coordinates of the six control points that represent the hole are the design variables. At the two control points whose coordinates are (0,0.1) and (0.1,0), the essential boundary conditions are imposed. Therefore, the two control points are fixed along the direction of their essential boundary conditions. The control point located at (0,0.1) can move vertically and the control point located at (0.1,0) can move horizontally during the shape optimization. Other four control points can move horizontally and vertically. It is well-known that stress is highly concentrated at point A in Fig. 20(a). Design objective of this problem is minimizing the maximum stress while total volume of the structure is maintained. As shown in Fig. 21, the initial concentration of stress is disappeared and smooth distribution of stress is obtained in the final design with 51% lower stress than the initial one.

5.3. A cantilever beam problem: compliance minimization with volume constraint

Many shape optimization problems including the previous two examples deal with very simple design problems: very small number of boundaries is movable, the amount of shape changes is relatively small and distortion of elements is not quite severe. Such simple examples can be treated by conventional FEM based shape optimization, even though the optimization process involved in the approach is rather troublesome and inefficient. In order to emphasize advantages of isogeometric analysis based shape optimization such as no parameterization and remeshing free process, more general problem should be treated: all movable boundaries and severe distortion of elements due to large amount of shape change. In this example, cantilever beam problem which is one of the most popular problems in structural optimization is chosen for numerical example. This problem is difficult to deal with conventional FEM based shape optimization since all boundaries are movable and the amount of shape change is almost unrestricted. In this example, T-spline local refinement and control point removal schemes are used to resolve geometric and numerical instabilities observed during optimization process.

5.3.1. Problem definition

A cantilever beam that is subjected to a concentrated force along the vertical direction is shown in Fig. 22(a). Compliance is minimized with 60% volume constraint of the initial design space in this example. Finite element model of the NURBS surface defined by the two knot spans, $\mathbf{s} = [0,0,0,0.2,0.4,0.6,0.8,1,1,1]$ and $\mathbf{t} = [0,0,0,0.25,0.5,0.75,1,1,1]$, 42 control points are shown in Fig. 22(b). The control points are initially classified by three cases as shown in Fig. 22(c). The control points marked by squares are design control points which can move along both directions. The control points marked by circles are concerned with boundary conditions and the concentrated force. In order to maintain horizontal dimension of the problem, they can move along the vertical direction only in the initial state. Some control points on the left side where essential boundary condition applied will be adaptively

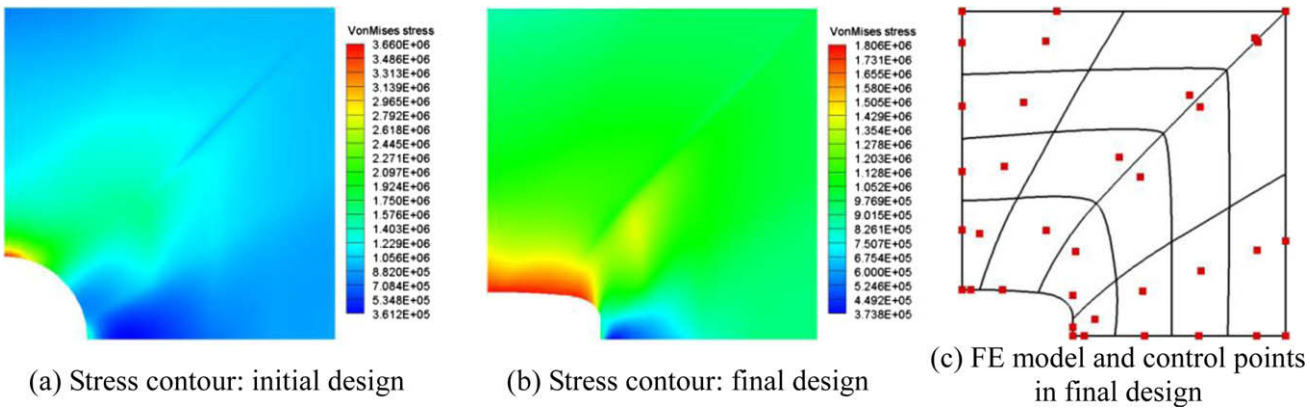

Fig. 21. Final design result: the hole design in a finite plate.

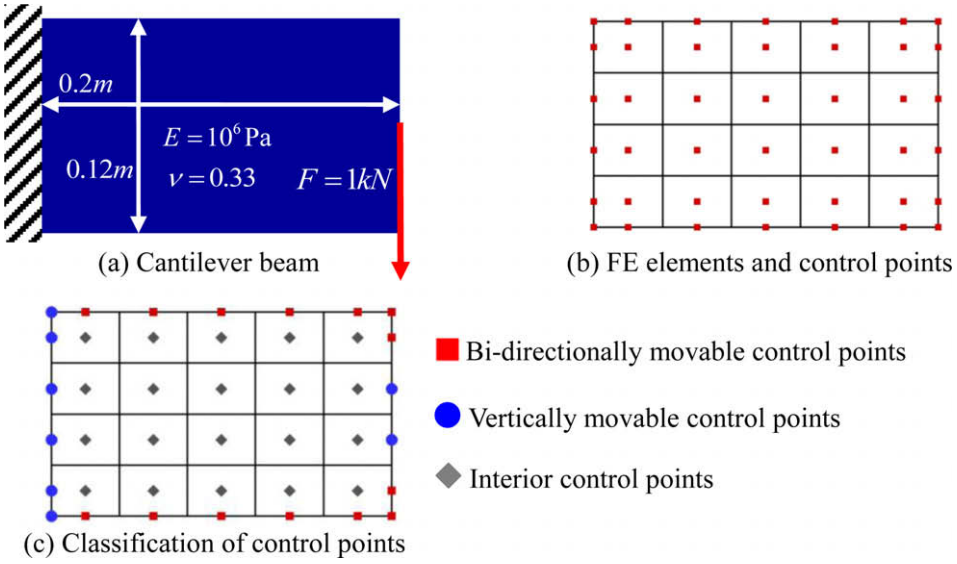

Fig. 22. Problem definition: the cantilever beam problem.

chosen as horizontally movable control points during optimization process to permit horizontal shape change of the boundary. The diamond shaped control points are located inside the boundaries. They are not design control points but they will move during the iterative process as the design control points move around. The movement of the interior control points can be determined by the boundary displacement method (Choi and Kim, 2005). The boundary displacement method will be explained in the following implementing issues of the proposed approach.

5.3.2. Implementing issues

In this example, there are three important implementing issues. The first one is boundary displacement method and the second one is an adaptive selection of movable design control points on the essential B. C. applied boundary. The last one is a special treatment of crowded design control points.

The boundary displacement method is employed to determine the movements of the interior control points. The determining process is realized by solving a separate linear elastic equation with the prescribed essential boundary conditions only. Fig. 23 shows boundary conditions for the boundary displacement method. The changes in design control points are imposed as additional essential boundary conditions.

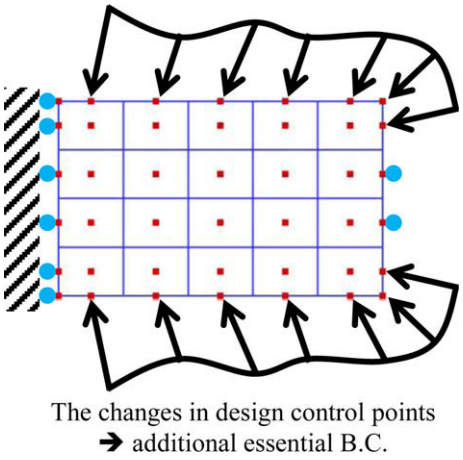

Fig. 23. Boundary conditions for boundary displacement method.

As mentioned above, in order to change the shape of the boundary under essential boundary condition, new design control points which can move along the horizontal direction should be adaptively selected during optimization process. For this, topological derivative is employed in this work. Topological derivative means difference in an objective function when a small hole is created and has been often employed for hole creation in level-set based topology optimization as mentioned in Section 1. In their works, a small hole is created at the location where topological derivative is the minimum value. In the same manner, in this example, topological derivative is used to determine new horizontally movable design control points on the left boundary. Topological derivative with respect to compliance is written as following equation (Garreau et al., 2001).

$$\Psi' = \frac{4\pi}{1+\nu}\boldsymbol{\sigma} : \boldsymbol{\varepsilon} + \frac{\pi(3\nu - 1)}{1-\nu^2} tr(\boldsymbol{\sigma}) \cdot tr(\boldsymbol{\varepsilon}) \tag{35}$$

When the minimum topological derivative is found at a certain point on the boundary, the control points whose compact support contains the minimum topological derivative position are determined. Fig. 24 illustrates how to select new design control points. The control points marked as circles in the right figure of Fig. 24 are selected as new design control points and then they are released horizontally to change the boundary shape. Note that the diamond shaped control points are introduced by T-spline local refinement using the knot multiplicity explained in Section 2. By repeating the two knot values, 0.25 and 0.75, in the original vertical knot, the diamond shaped control points are created at element corners. As shown in the figure, additional control points are created on the left boundary only by T-spline local refinement without global propagation to the whole surface. The diamond shaped control points are movable along the vertical direction only. Fig. 25 illustrates definitely different shapes when the diamond shaped control points are locally inserted on the left side or not. As shown in Fig. 25(a), if the diamond shaped control points are not inserted, as the control points marked as diamond move horizontally, the essential boundary condition is valid only at the bottom and top points of the left side. Moreover, the bottom and top corners of the left side become very sharp and tapered as iteration continues. Therefore, boundary condition and shape of the model become unstable unless the diamond control points are inserted. On the other hand, if the control points are inserted on the left side,

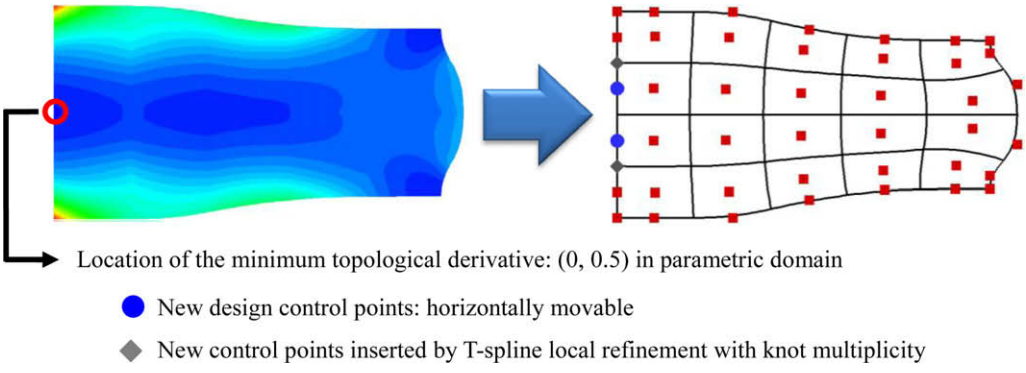

Fig. 24. Adaptive selection of design control points on the boundary where essential B.C applied.

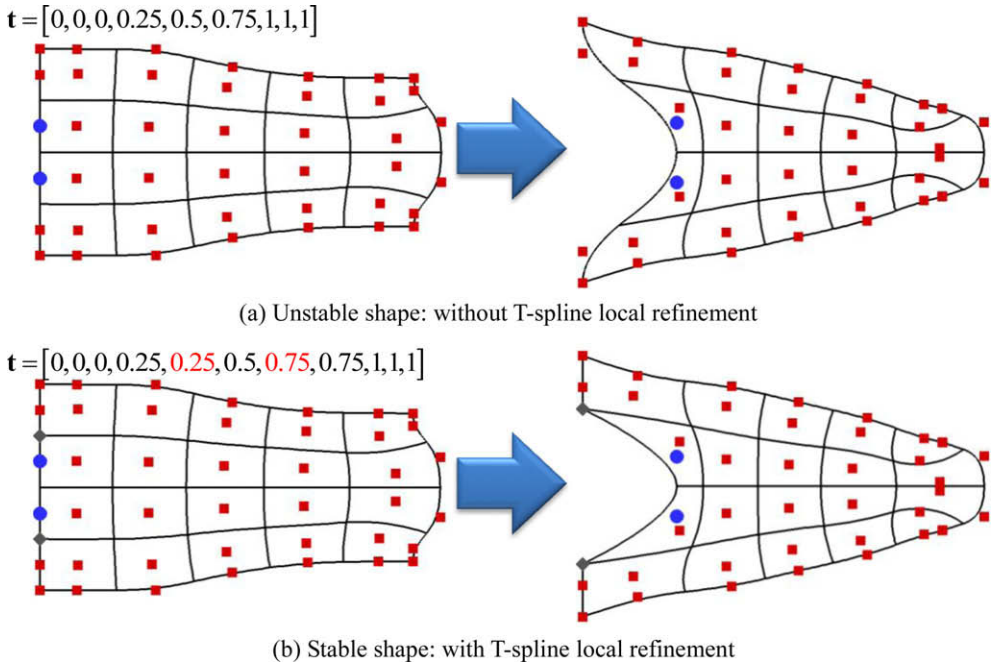

Fig. 25. Effect of locally inserted control points (diamond) on left side.

boundary condition is applied to reasonable area and structural shape is maintained stable (Fig. 25(b)). Since the control points are inserted by the knot multiplicity, continuity of the left side changes from C^1 to C^0 due to C^0 continuity and Kronecker-delta property of basis functions of the inserted control points.

During optimization process, some of the design control points may get crowded in a small area. They can be located at the nearly same position as shown in Fig. 26(a). Then, the movable space of the control points is restricted so that optimization process may become considerably slow and desired optimal solution may not be obtained. In the present work, the overlapped control points are removed to guarantee sufficient movable spaces of the design control points. For this, the two diamond control points on the right side which are nearly overlapped on other control points (Fig. 26(a)) will be removed from the design model by knot removal operation. Let us consider the two control points in the circle in Fig. 26(a). The local knot vectors corresponding to the control points are defined by the compact support of their basis functions. Therefore, the vertical knot vector of the diamond control point is [0.5, 0.75, 1, 1] and that of the square control point is [0.75, 1, 1, 1]. From the definition of B-spline, one knot value among the entities of the two knot vectors should be removed for removal of the diamond control point. Here, 0.75 and 1 are candidates for removing knot value. If the ending knots are removed, definition of B-spline basis function is violated: the ending knot should be repeated $(p+1)$ times in the open knot vector. Therefore, 0.75 should be removed from the vertical knot vector of the right side to remove the diamond control point. In the same way, 0.25 is also removed from the given vertical knot vector. Consequently, the vertical knot vector of the right side is changed from [0, 0, 0, 0.25, 0.5, 0.75, 1, 1, 1] to [0, 0, 0, 0.5, 1, 1, 1] and the number of control points along the side is also changed from six to four. As shown in Fig. 26(b), the elements on the right side are merged so that the side is divided into two elements. Since vertical knot span of the right side is not coincident with that of the left side after the knot removal on the side, the initial NURBS surface is no longer valid so that the parametric space of the surface is represented by T-mesh and T-spline interpolation is employed for later iterations in shape optimization.

5.3.3. Shape optimization results

Fig. 27 illustrates the iteration history of the model. As shown in the figure, design space is naturally expanded along the vertical direction so that two bar truss structure which is the optimum

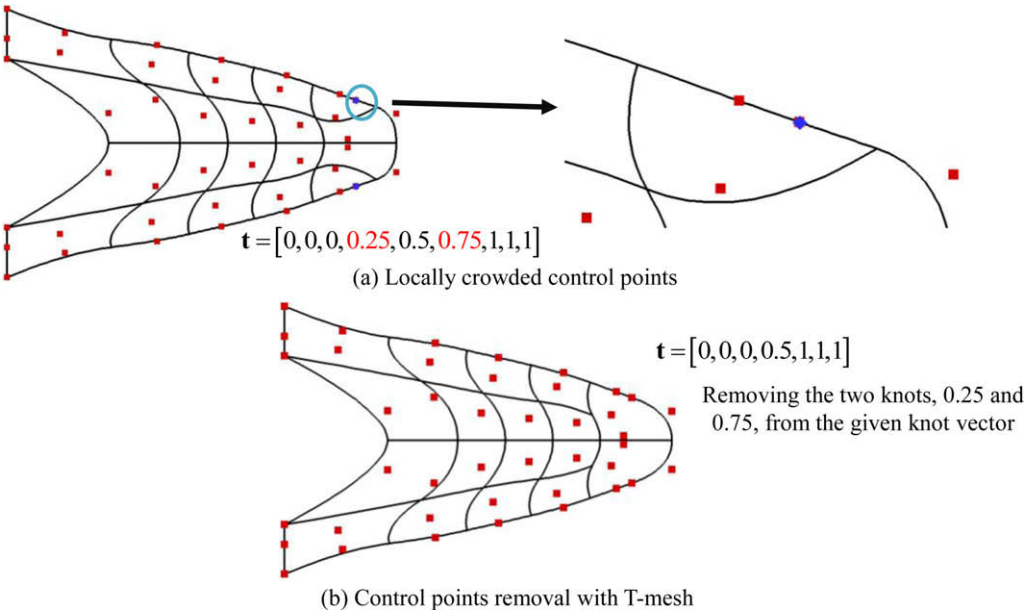

Fig. 26. Removal of the locally crowded control points: utilization of T-mesh.

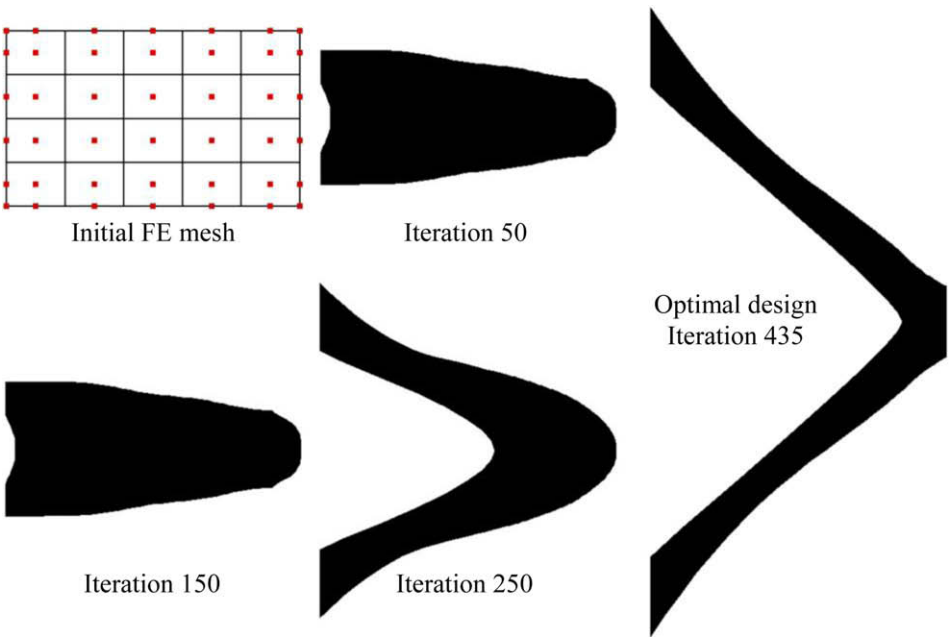

Fig. 27. Shape optimization: iteration history.

solution of the cantilever beam problem is easily obtained. The optimum solution is very difficult to obtain with the conventional shape optimization approaches even with topology optimization techniques. Although, expansion of the design space was attempted in some topology optimization methods to obtain the optimum solution (Jang and Kwak, 2008), they require predetermined large number of computational finite elements along the vertical direction during the whole iterative process and additional schemes to decide whether change of design space is beneficial or not. However, in the proposed approach, design space is naturally expanded without any additional schemes.

The graph in Fig. 28 shows iteration history of the objective function (solid line) and constraint (dash line). In the first few iterations, volume is reduced toward the volume constraint and the objective function increases. After the volume constraint is satisfied, the objective function decreases monotonically, then we can obtain converged solution with stable process.

The same problem is also demonstrated with two different initial conditions to test independency on initial volume and FE mesh. In the first case, the initial volume is assumed to be same with the final one. In the second case, the design model is divided into 8 by 6 elements defined by following two knot vectors.

$\mathbf{s} = [0,0,0,1/8,1/4,3/8,1/2,5/8,3/4,7/8,1,1,1]$ and
$\mathbf{t} = [0,0,0,1/6,1/3,1/2,2/3,5/6,1,1,1]$

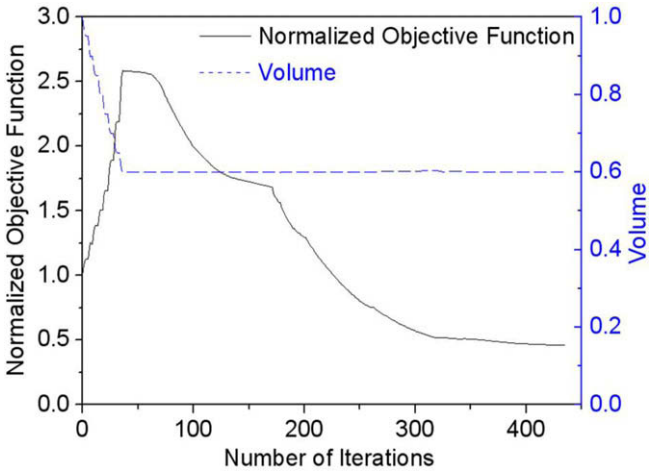

Fig. 28. Iteration history of the objective function and constraint.

Iteration histories of both cases are shown in Figs. 29 and 30, respectively. Optimal two bar truss structures are also obtained despite different initial conditions. Table 3 shows numerical results and computation time in the three cases studied here. As shown in the table, compliances of the three cases are very close and computational times are reasonably small although relatively large computation time is spent in the third case due to large number of iterations.

5.4. Application to shell problems

Shape optimization framework based on the isogeometric analysis can be easily applied to shell problems. Recently, the studies on the isogeometric analysis of shell structures were presented by several authors (Uhm and Youn, 2009; Kiendl et al., 2009; Benson et al., 2010). Main challenge of the isogeometric analysis of shells lies in defining normal vector of each control point. The control points do not lie on the surface whereas normal vectors are defined on the surface (Uhm and Youn, 2009). One reasonable way to define the normal vectors of the control points is to take the normal vectors at the projection points of the control points on the surface. The projection points corresponding to control points are determined by the point projection algorithm (Piegl and Tiller, 1997). Then, a normal vector at the projection point whose parameter is (s_i, t_i) is defined as follow:

$$\mathbf{V_3} = \begin{Bmatrix} l_3 \\ m_3 \\ n_3 \end{Bmatrix} = \frac{\mathbf{S}_{,s}(s_i,t_i) \times \mathbf{S}_{,t}(s_i,t_i)}{|\mathbf{S}_{,s}(s_i,t_i) \times \mathbf{S}_{,t}(s_i,t_i)|} \tag{36}$$

In this example, degenerate shell formulation based on Reissner–Mindlin shell theory for the isogeometric analysis (Uhm and Youn, 2009) is employed.

For shape optimal design of shell structures, the coordinates of control points are employed as design variables. In two dimensional problems, only boundary control points are design control points but in shape optimization of shells, all control points are design control points. Shape sensitivity analysis can be performed in a similar way described in Section 4. The element stiffness matrix of a shell element and its sensitivity with respect to design variables are written as follows.

$$\begin{aligned} \mathbf{k_e} &= \int \mathbf{B}^{\mathbf{T}}\mathbf{D}\mathbf{B}d\Omega = \int_{-1}^{1}\int_{-1}^{1}\int_{-1}^{1} \mathbf{B}^{\mathbf{T}}\mathbf{D}\mathbf{B}|\mathbf{J}|d\xi\, d\eta\, d\varsigma = \sum_{k=1}^{NINT} \mathbf{B}_k^{\mathbf{T}}\mathbf{D}\mathbf{B}_k|\mathbf{J}_k|W_k \\ \frac{\partial \mathbf{k_e}}{\partial \mathbf{x}} &= \sum_{k=1}^{NINT}\left[\frac{\partial \mathbf{B}_k^{\mathbf{T}}}{\partial \mathbf{x}}\mathbf{D}\mathbf{B}_k|\mathbf{J}_k|W_k + \mathbf{B}_k^{\mathbf{T}}\mathbf{D}\frac{\partial \mathbf{B}_k}{\partial \mathbf{x}}|\mathbf{J}_k|W_k + \mathbf{B}_k^{\mathbf{T}}\mathbf{D}\mathbf{B}_k\frac{\partial |\mathbf{J}_k|}{\partial \mathbf{x}}W_k\right] \end{aligned} \tag{37}$$

Strain-displacement matrix $\mathbf{B}$ is given by $\mathbf{B} = \mathbf{T}\mathbf{M}\Gamma\mathbf{G}$. $\mathbf{T}$ is the coordinate transformation matrix and the components of $\mathbf{G}$ are written in terms of the derivatives of basis functions and the normal vectors of control points. Since matrices $\mathbf{T}$, Γ and $\mathbf{G}$ are dependent on the design variables in shell elements, the derivative of $\mathbf{B}$ with respect to the design variables is written as

$$\frac{\partial \mathbf{B}}{\partial \mathbf{x}} = \frac{\partial \mathbf{T}}{\partial \mathbf{x}}\mathbf{M}\Gamma\mathbf{G} + \mathbf{T}\mathbf{M}\left(\frac{\partial \Gamma}{\partial \mathbf{x}}\mathbf{G} + \Gamma\frac{\partial \mathbf{G}}{\partial \mathbf{x}}\right) \tag{38}$$

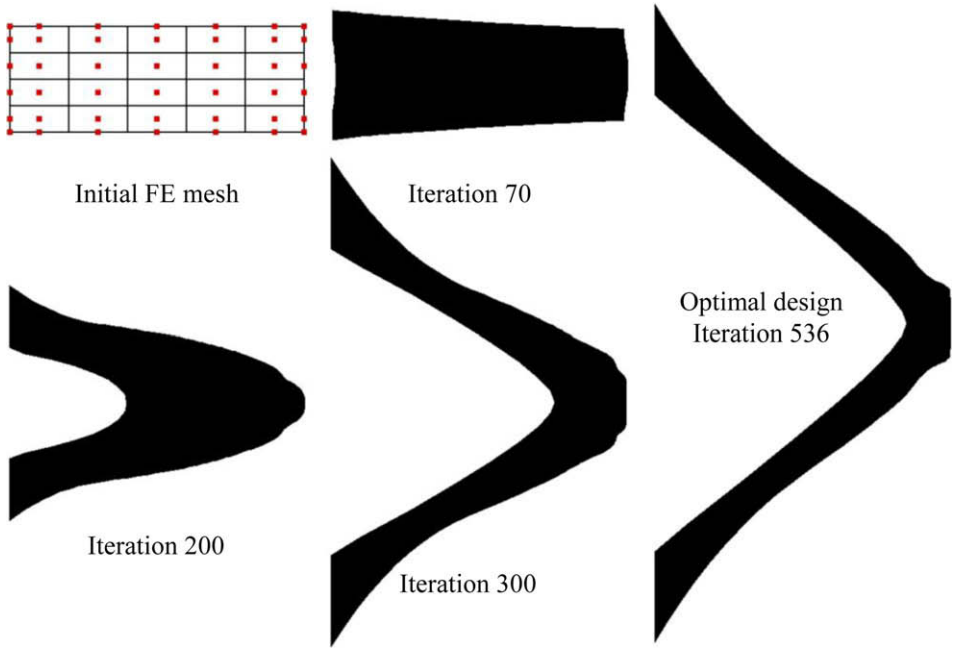

Fig. 29. Iteration history of the shape: the same initial volume with the final one.

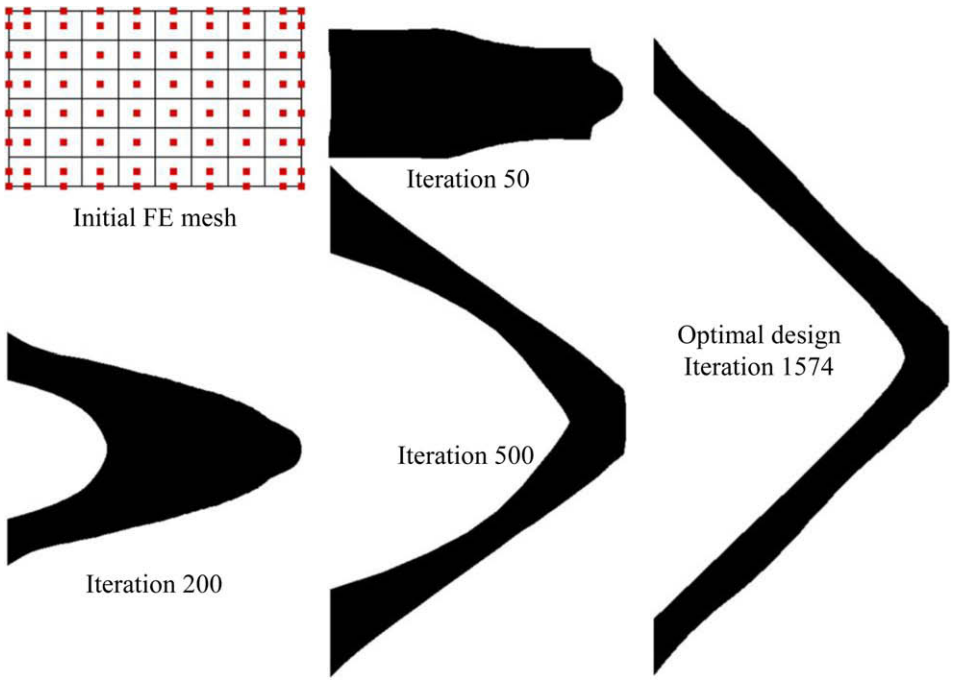

Fig. 30. Iteration history of the shape: different initial FE mesh.

Table 3
Numerical results of shape optimization according to the three different initial conditions.

Case	Mesh	Initial volume (%)	Final volume (%)	Compliance (Nm)	Number of Iteration	Time (s)
1	5×4	100	60	10.970	435	14.56
2	5×4	60		11.171	536	17.64
3	8×6	100		11.047	1574	63.36

Jacobian $\mathbf{J}$ is the same form with Eq. (12) but 3 by 3 matrix in shell elements.

$$\mathbf{J} = \mathbf{J_R}\mathbf{J_S} = \begin{bmatrix} \frac{s_{i+1}-s_i}{2} & 0 & 0 \\ 0 & \frac{t_{j+1}-t_j}{2} & 0 \\ 0 & 0 & 1 \end{bmatrix} \begin{bmatrix} \frac{\partial x}{\partial s} & \frac{\partial y}{\partial s} & \frac{\partial z}{\partial s} \\ \frac{\partial x}{\partial t} & \frac{\partial y}{\partial t} & \frac{\partial z}{\partial t} \\ \frac{\partial x}{\partial \varsigma} & \frac{\partial y}{\partial \varsigma} & \frac{\partial z}{\partial \varsigma} \end{bmatrix}, \quad \frac{\partial |\mathbf{J}|}{\partial \mathbf{X}} = |\mathbf{J_R}| \frac{\partial |\mathbf{J_S}|}{\partial \mathbf{X}}, \quad (39)$$

By applying Eqs. (29) and (30) to (28), the sensitivity of the element stiffness matrix in shell elements can be calculated.

Fig. 31 shows two different initial shell structures to be optimized. The initial shape of the first one is a flat shell and the other is a part of spherical shell. Four corner points of both models are fixed and a concentrated force is applied at center point of the each shell. Compliance is minimized with volume constraint. For the same final volume, volume constraint of the flat shell is 60% and that of the spherical one is 54.3%, respectively. The material properties used are $E = 10^6$ and $\nu = 0.3$. Fig. 32 illustrates the optimal designs of the two different initial shapes. Table 4 shows the values of the initial and final objective functions. The initial compliances of the two shells are quite different since the rigidity along the load direction of the perfectly flat shell is much lower than that of the spherically curved shell. Despite such differences in the initial

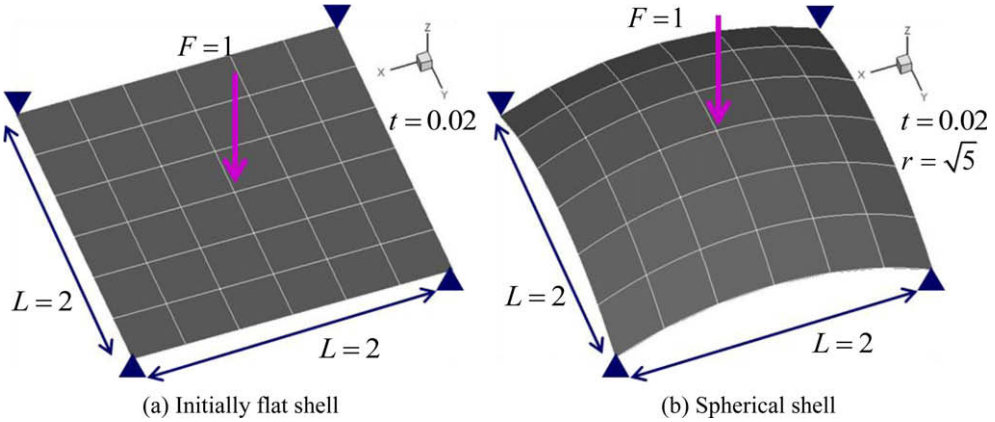

Fig. 31. Two different initial shells for shape optimization.

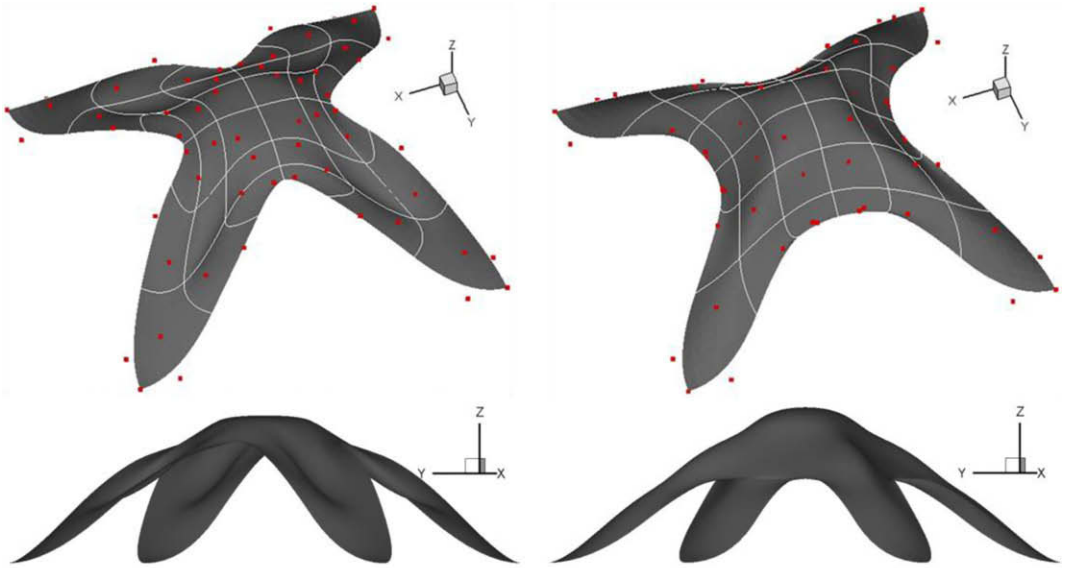

Fig. 32. Shape optimization of shells.

Table 4
Numerical results according to the two different initial conditions.

Initial shape	Initial compliance (Nm)	Final compliance (Nm)
Flat shell	77.329	0.374
Spherical shell	0.510	0.352

shapes and compliances, obtained optimal results are similar and the compliances of the optimal shapes are also very close to each other. As presented here, shape optimization of shells can be performed with the isogeometric analysis without any difficulty.

6. Extension of the proposed approach to topology optimization

6.1. A strategy for spline based topology optimization

The proposed spline based shape optimization can be readily extended to topological design using trimming techniques and the trimmed surface analysis explained in Section 3. As a first attempt to topology optimization based on the isogeometric analysis, the topological derivative in Eq. (35) is adopted as a measure for topological changes. If the point with the minimum topological derivative is inside design domain, a new inner front represented by a trimming spline curve is created around the point (Fig. 33). On the other hand, if the point with the minimum topological derivative is on boundaries, a new inner front is not created and shape optimization is carried out with the given topology. Trimming spline curves for representation of inner fronts are created in the parametric space since the numerical schemes in the trimmed surface analysis such as point inversion and integration cell decomposition are performed in the parametric space. The corresponding trimmed surface in the physical space is also shown in the figure. The trimming spline curve is defined by closed knot vector for its complete C^1 continuity. For example, the quadratic spline curve in Fig. 33 is defined by six control points and the closed knot vector $[-0.5,-0.25,0,0.25,0.5,0.75,1,1.25,1.5]$. Only four control points are shown in the figure since the coordinates of the last two control points are coincident with those of the first two control points. If trimming spline curves are introduced in the parametric space, the control points of the untrimmed surface in the physical space and those of the trimming curves in the parametric space are design control points. That is, the external boundaries are changed by the movements of the surface control points while the inner fronts are changed by the movements of the curve control points in the parametric space. The analytic sensitivities of surface control points were already derived in Section 4. Sensitivities of curve control points are calculated by finite difference method (FDM) since analytic sensitivity of curve control points cannot be derived due to the use of the iterative point inversion scheme for integration

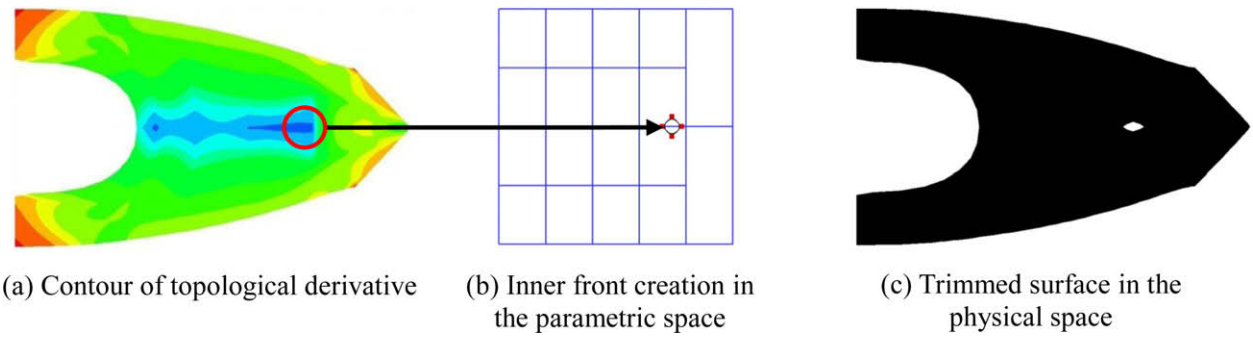

Fig. 33. A new inner front creation based on the topological derivative.

cell decomposition. Topology optimization in the present work terminates when the convergence criteria shown in Eq. (34) is satisfied and no more inner front is created. No more creation of inner front means that the point with the minimum topological derivative is on boundaries when the relative difference in the objective function satisfies the criteria in Eq. (34).

6.2. Numerical examples on topology optimization based on the trimmed surface analysis

The cantilever beam problem in Fig. 22 is also treated to demonstrate the proposed approach. Expansion of design space is not taken into account in this example. The issues explained in Section 5.3 are also implemented here. Fig. 34 shows the iteration histories of the objective function, constraint and topology of the model. From the initial shape, the outer boundaries are optimized by changing the coordinates of the surface control points until a new inner front is created based on the topological derivative. Once the inner fronts are created, the outer boundaries as well as the inner fronts are simultaneously optimized. For shape optimization of the inner fronts, the side constraints of the design control points of the trimming curves are determined in the same way shown in Fig. 17. In Fig. 34, topology changes in the physical surfaces and the parametric spaces are shown. The first change in the parametric space is the use of T-mesh due to the control points removal using T-splines explained in Section 5.3. After some iterations, new inner fronts are created sequentially by introducing trimming spline curves and the integration cells are decomposed in the parametric space for the trimmed surface analysis. As shown in the figure, arbitrary complex topologies can be easily treated by the trimmed surface analysis. Fig. 35 shows reasonable final topologies for different initial conditions: different initial distribution of control points and volume.

6.3. Discussions and further studies on spline based topology optimization

This work is the first exploration to topology optimization based on the isogeometric analysis. The proposed approach has a potential to be fully integrated shape and topology optimization based on splines. However, it has still some challenges to be settled. The first one is reducing computational time and the second one is more systematic strategy for topological changes.

Numerical results of topology optimization are shown in Table 5. As shown in the table, much more computational time is spent in topology optimization than that in shape optimization in Table 3.

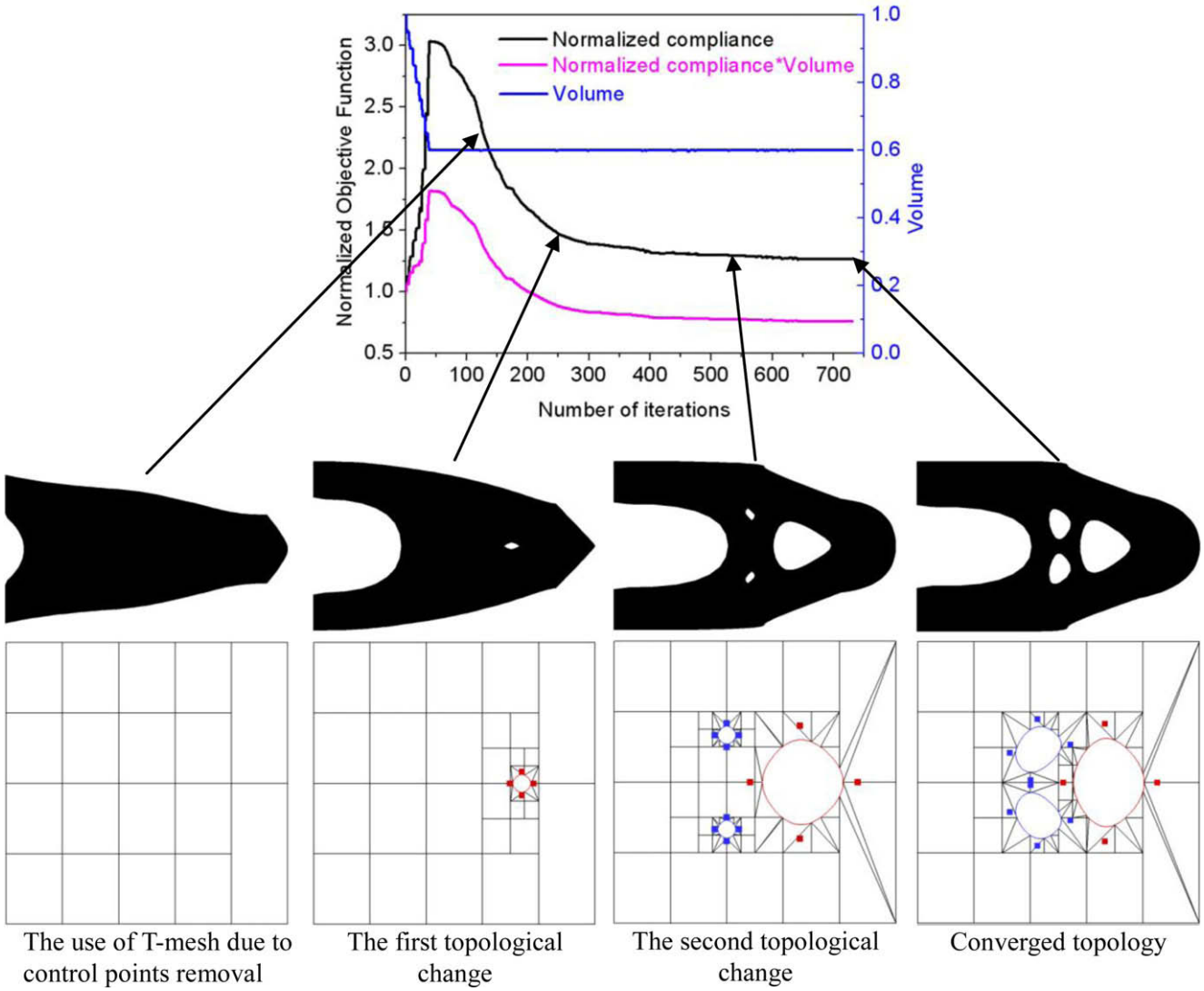

Fig. 34. Iteration history of cantilever beam problem: topology changes in the physical and the parametric spaces.

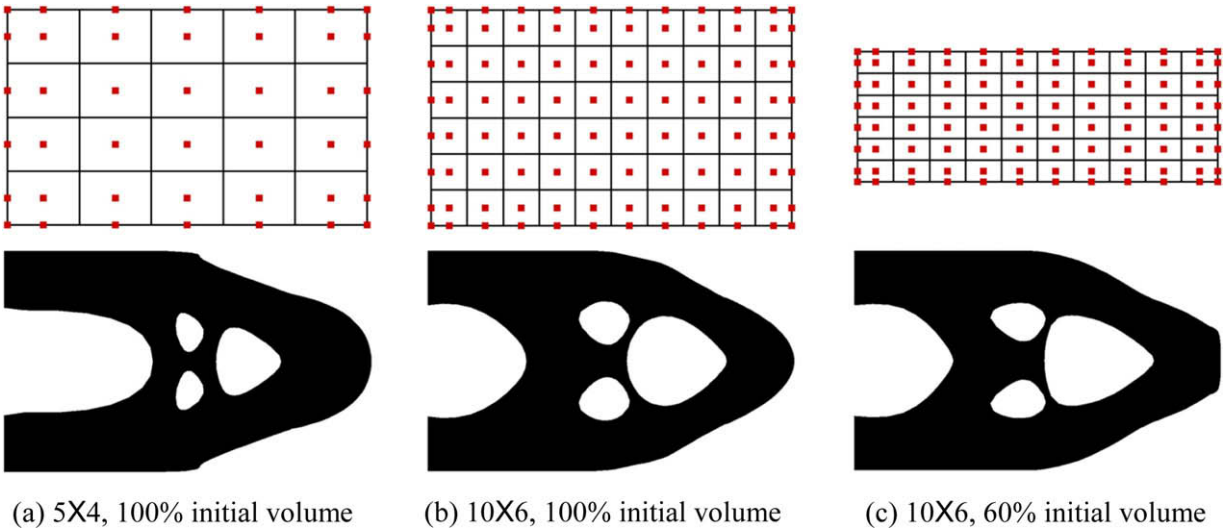

Fig. 35. Final topologies according to three different initial conditions.

Table 5
Numerical results of topology optimization according to the three different initial conditions.

Case	Mesh	Initial volume (%)	Final volume (%)	Compliance (Nm)	Number of iteration	Time (s)
1	5×4	100	60	29.932	731	343.7
2	10×6	100		32.300	660	295.6
3	10×6	60		32.220	951	376.0

Actually, most of time, about 90% of overall time, was elapsed after new inner fronts were created. Main reason on such high computational time in topology optimization is FDM calculation for sensitivities of the design control points of trimming curves. For FDM calculation, the trimmed surface analysis should be repeated for the sensitivities of every design control points of trimming curves. As the number of trimming curve increases, much more computational time is spent in topological design. In order to reduce computational time, a further investigation on an efficient sensitivity analysis is under investigation.

The strategy used in the present work for topology optimization is similar to that in the bubble method explained in Section 1. In the bubble method, bubbles are inserted into structures based on the characteristic function which is expressed in terms of stresses. Since the outer boundaries and inner bubbles are represented splines, the control points which represent the outer boundaries and inner bubbles are design variables. Then shape optimization is performed with the conventional FEM by remeshing the design model at each iteration. It was the earliest attempt which uses splines in topology optimization but its optimization process is quite inefficient in time due to remeshing and there is an ambiguity in the number of bubbles inserted. Furthermore, it does not permit insertion of additional bubbles during shape optimization of the bubbles which were already inserted. Such topological inflexibility may lead unexpected optimal design. Similarly, the drawbacks in the bubble method may be also appeared in our approach. Therefore, more flexible and systematic strategy for topological changes should be addressed to obtain better optimal design and it is also under investigation.

7. Conclusions and further works

In the present work, isogeometric analysis based shape and topology optimization are presented. The unification of the mathematical languages in design and analysis resolves the inefficiencies and limitations which come from the use of the conventional FEM in structural optimization. Additional parameterization of design variables with finite element models is not necessary and remeshing is not required during entire optimization process. Also, design result is not restricted in the predetermined initial design space. Three representative examples in two dimension are treated with our approach: a fillet design, a hole design in a finite plate and a cantilever beam problem. Especially, in the cantilever beam problem, large amount of change in shape is readily treated without any remeshing scheme and the local properties of T-splines are utilized to resolve the geometric and numerical instabilities. Two-bar truss structure that is the global optimum solution of the cantilever beam problem is successfully obtained with the proposed approach based on isogeometric analysis. Moreover, the shape optimization framework based on the isogeometric analysis has been directly extended to shell problems without any additional scheme and difficulty. As the first attempt to topological design based on the isogeometric analysis, the proposed approach is applied to topology optimization using trimming techniques and the trimmed surface analysis. Topological changes in spline surfaces are represented by trimming spline curves and arbitrary complex topologies can be easily treated by the trimmed surface analysis. The new framework for topology optimization has been demonstrated by applying the benchmarking problems.

As mentioned in Section 6.3, the proposed approach for topology optimization has challenges in sensitivity calculation and topological flexibility. In order to improve the proposed method, a new sensitivity formulation for design control points of trimming curves will be proposed for computational efficiency. A systematic algorithm for inner front creation and merging will be also given. Several benchmarking examples will be treated to demonstrate our approach and special advantages will be addressed.

Acknowledgement

This work was supported by the Korea Research Foundation Grant funded by the Korean Government OEHRD, Basic Research Promotion Fund) (KRF-2007-313-D00024).

References

Allaire, G., Jouve, F., 2005. A level-set method for vibration and multiple loads structural optimization. Computer Methods in Applied Mechanics and Engineering 194, 3269–3290.

Allaire, G., Jouve, F., Toader, A.M., 2004. Structural optimization using sensitivity analysis and a level set method. Journal of Computational Physics 194, 363–393.

Amstutz, S., Andra, H., 2006. A new algorithm for topology optimization using a level set method. Journal of Computational Physics 216, 573–588.

Bazilevs, Y., Calo, V.M., Cottrell, J.A., Hughes, T.J.R., Reali, A., Scovazzi, G., 2007. Variational multiscale residual-based turbulence modeling for large eddy simulation of incompressible flows. Computer Methods in Applied Mechanics and Engineering 197, 173–201.

Bazilevs, Y., Calo, V.M., Cottrell, J.A., Evans, J.A., Hughes, T.J.R., Lipton, S., Scott, M.A., Sederberg, T.W., 2010. Isogeometric analysis using T-splines. Computer Methods in Applied Mechanics and Engineering 199, 229–263.

Belytschko, T., Xiao, S.P., Parimi, C., 2003. Topology optimization with implicit functions and regularization. International Journal for Numerical Methods in Engineering 57, 1177–1196.

Bendsoe, M.P., Kikuchi, N., 1988. Generating optimal topologies in structural design using a homogenization method. Computer Methods in Applied Mechanics and Engineering 71, 197–224.

Bendsoe, M.P., Sigmund, O., 1999. Material interpolation schemes in topology optimization. Archieve of Applied Mechanics 69, 635–654.

Bendsoe, M.P., Sigmund, O., 2003. Topology Optimization – Theory Methods, and Applications. Springer-Verlag, Berlin.

Bennet, J., Botkin, M., 1984. Structural shape optimization with geometric problem description and adaptive mesh refinement. AIAA Journal 23, 458–464.

Benson, D.J., Bazilevs, Y., Hsu, M.C., Hughes, T.J.R., 2010. Isogeometric shell analysis: the Reissner–Mindlin shell. Computer Methods in Applied Mechanics and Engineering 199, 276–289.

Bhavikatti, S.S., Ramakrishnan, C.V., 1980. Optimum shape design of rotating disks. Computers and Structures 11, 397–401.

Borrvall, T., 2001. Topology optimization of elastic continua using restriction. Archives of Computational Methods in Engineering 8, 351–385.

Bourdin, B., 2001. Filters in topology optimization. International Journal for Numerical Methods in Engineering 50, 2143–2158.

Braibant, V., Fleury, C., 1984. Shape optimal design using b-splines. Computer Methods in Applied Mechanics and Engineering 44, 247–267.

Bruns, T.E., Tortorelli, D.A., 2001. Topology optimization of non-linear elastic structures and compliant mechanisms. Computer Methods in Applied Mechanics and Engineering 190, 3443–3459.

Burger, M., Hackl, B., Ring, W., 2004. Incorporating topological derivatives into level set methods. Journal of Computational Physics 194, 344–362.

Cervera, E., Trevelyan, J., 2005. Evolutionary structural optimisation based on boundary representation of NURBS. Part I: 2D algorithms. Computers and Structures 83, 1902–1916.

Chang, S.Y., Youn, S.K., 2006. Material cloud method for topology optimization. International Journal for Numerical Methods in Engineering 65 (10), 1585–1607.

Cho, S., Ha, S.H., 2009. Isogeometric shape design optimization: exact geometry and enhanced sensitivity. Structural and Multidisciplinary Optimization 38 (1), 53–70.

Cho, M., Roh, H.Y., 2003. Development of geometrically exact new shell elements based on general curvilinear coordinates. International Journal for Numerical Methods in Engineering 56, 81–115.

Choi, K.K., Kim, N.H., 2005. Structural Sensitivity Analysis and Optimization 2: Nonlinear Systems and Applications. Springer, New York.

Cottrell, J.A., Reali, A., Bazilevs, Y., Hughes, T.J.R., 2006. Isogeometric analysis of structural vibrations. Computer Methods in Applied Mechanics and Engineering 195, 5257–5296.

Cottrell, J.A., Hughes, T.J.R., Reali, A., 2007. Studies of refinement and continuity in isogeometric structural analysis. Computer Methods in Applied Mechanics and Engineering 196, 4160–4183.

Ding, Y., 1986. Shape optimization of structures: a literature survey. Computers and Structures 24, 985–1004.

Dörfel, M.R., Jüttler, B., Simeon, B., 2010. Adaptive isogeometric analysis by local h-refinement with T-splines. Computer Methods in Applied Mechanics and Engineering 199, 264–275.

Eschenauer, H.A., Kobelev, V.V., Schumacher, A., 1993. Bubble method for topology and shape optimization of structures. Structural Optimization 8, 42–51.

Francavilla, A., Ramakrishnan, C.V., Zienkiewicz, O.C., 1975. Optimization of shape to minimize stress concentration. The Journal of Strain Analysis for Engineering Design 10, 63–70.

Garreau, S., Guillaume, P., Masmoudi, M., 2001. The topological asymptotic for PDE systems: the elasticity case. SIAM Journal on Control and Optimization 39 (6), 1756–1778.

Guo, X., Gu, Y.X., 2004. A new density stiffness interpolation scheme for topology optimization of continuum structures. Engineering Computations 21, 9–22.

Haber, R.B., Jog, C.S., Bendsoe, M.P., 1996. A new approach to variable-topology shape design using a constraint on perimeter. Structural Optimization 11, 1–12.

Haftka, R.T., Grandhi, R.V., 1986. Structural shape optimization – a survey. Computer Methods in Applied Mechanics and Engineering 57, 91–106.

Hsu, Y.L., 1994. A review of structural shape optimization. Computers in Industry 26, 3–13.

Hughes, T.J.R., Cottrell, J.A., Bazilevs, Y., 2005. Isogeometric analysis: CAD, finite elements, NURBS, exact geometry and mesh refinement. Computer Methods in Applied Mechanics and Engineering 194, 4135–4195.

Imam, M.H., 1982. Three-dimensional shape optimization. International Journal for Numerical Methods in Engineering 18, 661–673.

Jang, I.K., Kwak, B.M., 2008. Design space optimization using design space adjustment and refinement. Structural and Multidisciplinary optimization 35, 41–54.

Kagan, P., Fischer, A., Bar-Yoseph, P.Z., 1998. New B-spline finite element approach for geometrical design and mechanical analysis. International Journal for Numerical Methods in Engineering 41, 435–458.

Kiendl, J., Bletzinger, K.U., Linhard, J., Wüchner, R., 2009. Isogeometric shell analysis with Kirchhoff–Love elements. Computer Methods in Applied Mechanics and Engineering 198, 3902–3914.

Kim, N.H., Chang, Y., 2005. Eulerian shape design sensitivity analysis and optimization with a fixed grid. Computer Methods in Applied Mechanics and Engineering 194, 3291–3314.

Kim, H., Xie, O.M., Steven, G.P., Xie, Y.M., 2003. Improving efficiency of evolutionary structural optimization by implementing fixed grid mesh. Structural and Multidisciplinary Optimization 24, 441–448.

Kim, H.J., Seo, Y.D., Youn, S.K., 2009. Isogeometric analysis for trimmed CAD surfaces. Computer Methods in Applied Mechanics and Engineering 198, 2982–2995.

Lee, S.B., Kwak, B.M., Kim, I.Y., 2007. Smooth boundary topology optimization using B-spline and hole generation. International Journal of CAD/CAM 7 (2).

Natekar, D., Zhang, X., Subbarayan, G., 2004. Constructive solid analysis: a hierarchical, geometry-based meshless analysis procedure for integrated design and analysis. Computer-Aided Design 36, 473–486.

Park, K.S., Youn, S.K., 2008. Topology optimization of shell structures using adaptive inner-front (AIF) level set method. Structural and Multidisciplinary Optimization 36 (1), 43–58.

Pedersen, P., Laursen, C.L., 1983. Design for minimum stress concentration by finite elements and linear programming. Journal of Structural Mechanics 10, 375–391.

Petersson, J., Sigmund, O., 1998. Slope constrained topology optimization. International Journal for Numerical Methods in Engineering 41 (8), 1417–1434.

Piegl, L., Tiller, W., 1997. The NURBS Book, second ed. Springer, New York.

Querin, O.M., Xie, Y.M., Steven, G.P., 1998. Evolutionary structural optimization (ESO) using a bi-directional algorithm. Engineering Computations 15, 1031–1048.

Rayasam, M., Srinivasan, V., Subbarayan, G., 2007. CAD inspired hierarchical partition of unity constructions for NURBS-based, meshless design, analysis and optimization. International Journal for Numerical Methods in Engineering 72, 1452–1489.

Roh, H.Y., Cho, M., 2004. The application of geometrically exact shell elements to B-spline surfaces. Computer Methods in Applied Mechanics and Engineering 193, 2261–2299.

Roh, H.Y., Cho, M., 2005. Integration of geometric design and mechanical analysis using B-spline functions on surface. International Journal for Numerical Methods in Engineering 62, 1927–1949.

Rozvany, G.I.N., Zhou, M., Birker, T., 1992. Generalized shape optimization without homogenization. Structural Optimization 4, 250–252.

Sederberg, T.W., Zheng, J., Bakenov, A., Nasri, A., 2003. T-splines and T-NURCCs. ACM Transactions on Graphics 22, 477–484.

Sederberg, T.W., Cardon, D.L., Finnigan, G.T., North, N.S., Zheng, J., Lyche, T., 2004. T-spline simplification and local refinement. ACM Transactions on Graphics 23, 276–283.

Seo, Y.D., Youn, S.K., 2008. Integrated Structural Optimization with T-Spline Finite Element Method (TSFEM). WCCM8, Venice, Italy, June–July.

Sethian, J.A., Wiegmann, A., 2000. Structural boundary design via level set and immersed interface method. Journal of Computational Physics 163, 489–528.

Sevilla, R., Fernández-Méndez, S., Huerta, A., 2008. NURBS-enhanced finite element method (NEFEM). International Journal for Numerical Methods in Engineering 76 (1), 56–83.

Sigmund, O., Petersson, J., 1998. Numerical instabilities in topology optimization: a survey on procedures dealing with checkerboards, mesh-dependencies and local minima. Structural Optimization 16, 68–75.

Svanberg, K., 1987. The method of moving asymptotes – a new method for structural optimization. International Journal for Numerical Methods in Engineering 24, 359–373.

Uhm, T.K., Youn, S.K., 2009. T-spline finite element method for the analysis of shell structures. International Journal for Numerical Methods in Engineering 80, 507–536.

Uhm, T.K., Kim, K.S., Seo, Y.D., Youn, S.K., 2008. A locally refinable T-spline finite element method for CAD/CAE integration. Structural Engineering and Mechanics 30, 225–245.

Wall, W.A., Frenzel, M.A., Cyron, C., 2008. Isogeometric structural shape optimization. Computer Methods in Applied Mechanics and Engineering 197, 2976–2988.

Wang, M.Y., Wang, X.M., 2004. Color level sets: a multi-phase level set method for structural topology optimization with multiple materials. Computer Methods in Applied Mechanics and Engineering 193, 469–496.

Wang, M.Y., Wang, X.M., Guo, D.M., 2003. A level set method for structural topology optimization. Computer Methods in Applied Mechanics and Engineering 192, 227–246.

Wang, M.Y., Wang, X.M., Guo, D.M., 2004. Structural shape and topology optimization in a level-set based framework of region representation. Structural and Multidisciplinary Optimization 27, 1–19.

Wilke, D., Kok, S., Groenwold, A., 2006. A quadratically convergent unstructured remeshing strategy for shape optimization. International Journal for Numerical Methods in Engineering 65, 1–17.

Xie, Y.M., Steven, G.P., 1993. A simple evolutionary procedure for structural optimization. Computers and Structures 49, 885–896.

Xie, Y.M., Steven, G.P., 1994. Optimal design of multiple load case structures using an evolutionary procedure. Engineering Computations 11, 295–302.

Yoon, G.H., Kim, Y.Y., 2005. Element connectivity parameterization for topology optimization of geometrically nonlinear structures. International Journal of Solids and Structures 42 (7), 1983–2009.

Youn, S.K., Park, S.H., 1997. A study on the shape extraction process in the structural topology optimization using homogenized material. Computers and Structures 62 (3), 527–538.

Zhang, X., Rayasam, M., Subbarayan, G., 2007a. A meshless, compositional approach to shape optimal design. Computer Methods in Applied Mechanics and Engineering 196, 2130–2146.

Zhang, Y., Bazilevs, Y., Goswami, S., Bajaj, C.L., Hughes, T.J.R., 2007b. Patient-specific vascular NURBS modeling for isogeometric analysis of blood flow. Computer Methods in Applied Mechanics and Engineering 196, 2943–2959.

Zhou, M., Shyy, Y.K., Thomas, H.L., 2001. Checkerboard and minimum member size control in topology optimization. Structural and Multidisciplinary Optimization 21, 152–158.